Mon. Not. R. Astron. Soc. **396,** 141–164 (2009) doi:10.1111/j.1365-2966.2009.14742.x

The impact of feedback on disc galaxy scaling relations

Aaron A. Dutton[1,2★] and Frank C. van den Bosch[3]

[1] *UCO/Lick Observatory and Department of Astronomy and Astrophysics, University of California, Santa Cruz, CA 95064, USA*
[2] *Department of Physics, Swiss Federal Institute of Technology (ETH Zürich), CH-8093 Zürich, Switzerland*
[3] *Max-Planck-Institut für Astronomie, Königstuhl 17, 69117 Heidelberg, Germany*

Accepted 2009 March 3. Received 2009 January 31; in original form 2008 October 18

ABSTRACT

We use a disc galaxy evolution model to investigate the impact of mass outflows (a.k.a. feedback) on disc galaxy scaling relations, mass fractions and spin parameters. Our model follows the accretion, cooling, star formation and ejection of baryonic mass inside growing dark matter haloes, with cosmologically motivated angular momentum distributions, and dark matter halo structure. Models without feedback produce discs that are too small, too gas-poor and which rotate too fast. Feedback reduces the galaxy formation efficiency $\epsilon_{\rm GF}$ (defined as the fraction of the universally available baryons that end up as stars and cold gas in a given galaxy), resulting in larger discs with higher gas fractions and lower rotation velocities. Models with feedback can reproduce the zero-points of the scaling relations among rotation velocity, stellar mass and disc size, but only in the absence of adiabatic contraction. Our feedback mechanism is maximally efficient in expelling mass, but our successful models require 25 per cent of the supernova (SN) energy or 100 per cent of the SN momentum to drive an outflow. It remains to be seen whether such high efficiencies are realistic or not. Our energy- and momentum-driven wind models result in different slopes of various scaling relations. Energy-driven winds result in steeper slopes to the galaxy-mass–halo-mass and stellar-mass–halo-mass relations, a shallower slope to the galaxy-size–stellar-mass relation at $z = 0$ and a steeper slope to the cold gas metallicity–stellar-mass relation at $z \simeq 2$. Observations favour the energy-driven wind at stellar masses below $M_{\rm star} \lesssim 10^{10.5}\,{\rm M}_\odot$, but the momentum-driven wind model at high masses. The ratio between the specific angular momentum of the baryons to that of the halo ($j_{\rm gal}/m_{\rm gal}$) is not unity in our models with inflow and outflow. Yet this is the standard assumption in models of disc formation. Above a halo mass of $M_{\rm vir} \simeq 10^{12}\,{\rm M}_\odot$, cooling becomes increasingly inefficient, which results in ($j_{\rm gal}/m_{\rm gal}$) decreasing with increasing halo mass. Below a halo mass of $M_{\rm vir} \simeq 10^{12}\,{\rm M}_\odot$, feedback becomes increasingly efficient. Feedback preferentially ejects low-angular-momentum material because star formation is more efficient at smaller galactic radii and at higher redshifts. This results in ($j_{\rm gal}/m_{\rm gal}$) increasing with decreasing halo mass. This effect helps to resolve the discrepancy between the high spin parameters observed for dwarf galaxies with the low spin parameters predicted from Λ cold dark matter.

Key words: galaxies: formation – galaxies fundamental parameters – galaxies: haloes – galaxies: kinematics and dynamics – galaxies: spiral – galaxies: structure.

1 INTRODUCTION

Understanding the origin and nature of galaxy scaling relations is a fundamental quest of any successful theory of galaxy formation. The success of a particular theory will be judged by its ability to reproduce the slope, scatter and zero-point of any robust galaxy scaling relation. Of particular interest are the scaling relations among size (R), luminosity (or stellar mass, M) (L) and velocity (V), as these parameters are related to each other via the virial theorem. For early-type galaxies, these three parameters are indeed coupled, resulting in a two-dimensional plane known as the Fundamental Plane (Djorgovski & Davis 1987; Dressler et al. 1987). However, for late-type galaxies, the relation between rotation velocity and luminosity, known as the Tully–Fisher (TF) relation (Tully & Fisher 1977), is independent of galaxy size or surface brightness (e.g. Courteau & Rix 1999; Courteau et al. 2007; Pizagno et al. 2007). Understanding the origin of this surface brightness independence is likely the key

★E-mail: dutton@ucolick.org

to understanding the small scatter of the TF, and may even explain the origin of the zero-point of the TF relation.

The slopes of the *VLR* relations for disc galaxies can be broadly understood with galaxy formation models that include virial equilibrium after dissipationless collapse of quasi-spherical cold dark matter (CDM) haloes and angular momentum conservation (e.g. Mo, Mao & White 1998, hereafter MMW; van den Bosch 1998, 2000; Firmani & Avila-Reese 2000; Navarro & Steinmetz 2000; Dutton et al. 2007, hereafter D07).

However, reproducing these scaling relations in detail has been a problem for galaxy formation models. To date, no (self-consistent) CDM-based model of galaxy formation can *simultaneously* match the zero-points of the TF relation, galaxy sizes and the luminosity (or stellar mass) function (e.g. Benson et al. 2003; D07). Models which match the zero-point of the TF relation do so by making the assumption that $V_{\rm rot}$, the observed rotation velocity, is equal to $V_{\rm vir}$, the circular velocity, at the virial radius (e.g. Somerville & Primack 1999) or $V_{\rm max,h}$, the maximum circular velocity of the halo prior to galaxy formation (e.g. Croton et al. 2006). For typical galaxy mass dark matter haloes $V_{\rm max,h}/V_{\rm vir} \simeq 1.1$ (e.g. Bullock et al. 2001a), so these two assumptions are almost equivalent. Other more observational approaches also support the conclusion that $V_{\rm rot} \simeq V_{\rm max,h}$ (Eke et al. 2006; Blanton, Geha & West 2008). The problem for the galaxy formation theory is that both cosmological simulations and analytic models of disc galaxy formation that take into account the self-gravity of the baryons and the effect of halo contraction (Blumenthal et al. 1986) find that $V_{\rm rot} \simeq 1.8\ V_{\rm vir}$ (Navarro & Steinmetz 2000; Abadi et al. 2003; D07; Governato et al. 2007).

Due to the almost one-to-one correlation between $V_{\rm max,h}$ and $M_{\rm vir}$, and the correlation between $V_{\rm rot}$ and baryonic $M_{\rm gal}$ mass (the baryonic TF relation e.g. McGaugh et al. 2000), an equivalent constraint to the ratio between $V_{\rm rot}$ and $V_{\rm max,h}$ is the galaxy mass fraction: $m_{\rm gal} = M_{\rm gal}/M_{\rm vir}$. Observations of halo masses using weak lensing (Hoekstra et al. 2005; Mandelbaum et al. 2006) find that for late-type galaxies the maximum $m_{\rm gal} \simeq 0.33\, f_{\rm bar}$, where $f_{\rm bar} = \Omega_{\rm b}/\Omega_{\rm m,0} \simeq 0.17$ is the cosmic baryon mass fraction at redshift zero. Similarly low galaxy formation efficiencies are obtained by methods that match the stellar mass function with the dark halo mass function (e.g. Yang et al. 2007; Conroy & Wechsler 2008).

A partial explanation for the surface brightness independence of the TF relation, or equivalently the weak correlation between residuals of the *VL* and *RL* relations, is that observationally (e.g. McGaugh & de Blok 1997) gas fractions correlate with surface brightness, with higher gas fractions in lower surface brightness galaxies. Since lower surface density discs are expected to rotate more slowly at a given baryonic mass, the larger gas fractions shift these galaxies to lower stellar masses and hence to lower luminosities (Firmani & Avila-Reese 2000; van den Bosch 2000). However, this solution is not very effective for the high-surface-brightness, low-gas-fraction galaxies. D07 showed that a reasonable amount of scatter in the stellar-mass-to-light ratios helps to reduce the correlation between the residuals of the *VL* and *RL* relations further. Gnedin et al. (2007) proposed a correlation between disc mass fraction and disc surface density to explain the lack of a correlation between the *VM* and *RM* relations.

Thus understanding the physical mechanisms that determine galaxy mass fractions is fundamental to our understanding of the origin of the *VLR* relations of disc galaxies. In the standard picture of disc galaxy formation, gas that enters the halo gets shock heated to the virial temperature, and then cools radiatively (Fall & Efstathiou 1980). Thus in order to produce low galaxy mass fractions, either a significant fraction of the gas has to be prevented from cooling or a significant fraction must subsequently be ejected from the disc and halo. The latest hydrodynamical simulations indicate that rather than accreting gas via a cooling flow, below a critical halo mass of $M_{\rm vir} \simeq 10^{12}\,{\rm M}_{\odot}$ gas does not shock as it enters the halo, and instead accretes straight on to the galaxy in a cold flow (Birnboim & Dekel 2003; Keres et al. 2005). In this scenario, essentially all of the baryons accrete on to the galaxy, and the problem of stopping the baryons from cooling becomes one of stopping the cold flows from forming. Thus in the absence of some kind of preheating (e.g. Mo et al. 2005) which would shut down the cold flows, mass outflows are required in order to produce the low galaxy mass fractions observed in the Universe today.

In order to investigate how mass outflows (a.k.a. feedback) determine galaxy mass fractions, and the impact this has on disc galaxy scaling relations, we use an updated version of the disc galaxy evolution models presented in van den Bosch (2001; 2002a). In these models, the input parameters are the concentration and spin of the dark matter halo. The galaxy spin parameter, galaxy mass fraction and gas to stellar mass ratio are collectively determined by the efficiencies of cooling, star formation (SF) and feedback.

The main differences with respect to the van den Bosch (2002a) models are as follows.

(i) We use cosmologically motivated specific angular momentum distributions (AMDs) of the halo gas rather than shells in solid body rotation.

(ii) We consider a SF recipe based on dense molecular gas rather than on total gas with a Toomre SF threshold.

(iii) We include scatter in halo concentration which we relate to the mass accretion history (MAH).

(iv) We explore two different feedback models: one based on kinetic energy conservation and the other based on momentum conservation.

An important aspect of this model is that we do not assume that the baryonic disc has an exponential density profile. In this model, the surface density profile of the baryonic disc is determined by detailed conservation of angular momentum, starting from the AMDs of gas haloes as found in cosmological simulations. The surface density profile of the stars is then determined by the relative efficiencies of SF, outflows and inflows as a function of radius. This allows us to self-consistently follow the evolution of the radial distributions of gas and stars. In future papers, we use this galaxy formation model to investigate the origin of disc galaxy surface density profiles (Dutton 2009) and the evolution of disc galaxy scaling relations.

This paper is organized as follows. In Section 2, we describe the disc galaxy formation models; in Section 3, we discuss the effect of feedback on the *VMR* relations; in Section 4, we discuss the impact of feedback on galaxy mass fractions and galaxy spin parameters; in Section 5, we discuss the effect of feedback on the mass–metallicity relation at $z \simeq 2$; in Section 6, we discuss how galaxies lose their gas and in Section 7 we give a summary.

2 DISC GALAXY FORMATION MODELS

The main assumptions that characterize the framework of our models are the following.

(i) Dark matter haloes around disc galaxies grow by the smooth accretion of mass.

(ii) The baryons acquire the same distribution of specific angular momentum as the dark matter.

(iii) Gas that enters the halo is shock heated to the virial temperature.

(iv) Gas cools conserving its specific angular momentum.

(v) SF occurs according to a Schmidt-type law on the dense molecular gas.

(vi) Supernova (SN) feedback reheats some of the cooled gas, ejecting it from the halo.

(vii) The halo contracts and expands adiabatically to inflows and outflows, respectively.

Each model galaxy consists of five mass components: dark matter, hot halo gas, disc mass in stars, disc mass in cold gas and ejected gas. The dark matter and the hot gas are assumed to be distributed in spherical shells, the disc mass is assumed to be in infinitesimally thin annuli. Throughout this paper, we refer to R as radius, t as time (where $t = 0$ is defined as the big bang) and z as redshift.

For each galaxy, we set up a radial grid with 200 bins quadratically sampled from 0.001 to 1 times the redshift zero virial radius, and follow the formation and evolution of the galaxy using 400 redshift steps quadratically sampled from $z = 10$ to 0. For each time-step, we compute the changes in the various mass components in each radial bin. The prescriptions we use are described in detail below.

2.1 Limitations of the model

Before we describe the details of the model, we first discuss the relevance of our model for understanding galaxy formation in a hierarchical universe.

The assumption of smooth mass accretion might seem inconsistent with the hierarchical merger picture of structure formation in a Λ CDM universe. However, major mergers of stellar rich galaxies are known to destroy discs (e.g. Barnes 1992; Cox et al. 2006), so disc galaxies are unlikely to form in haloes with recent major mergers. Minor mergers are more common than major mergers, and are likely to play an important role in the formation of galaxy bulges, either directly or by triggering secular processes. Thus by not including mergers our model underestimates bulge fractions. However, one of the goals of these models is to determine how much of the structural properties of disc galaxies can be accounted for with the 'zeroth-order' scenario of disc formation (smooth accretion and quiescent SF).

Our assumption about the way gas is accreted into galaxies (by a cooling flow of shock-heated gas) is likely incorrect. Simulations suggest that disc galaxies accrete most of their mass though cold flows, and that in the absence of extra heating or outflows the baryon fraction of galaxies is close to the universal value (Keres et al. 2005). In our model, the gas shock heats, but since for haloes with masses below $10^{12}\,\mathrm{M}_{\odot}$ the cooling time is short compared to the Hubble time, essentially all the gas that enters the halo accretes on to the disc in a free-fall time. Thus, although the physical mechanism by which galaxies accrete their gas in our model and cosmological simulations is different, we expect that the specific AMD of cold flow baryons to be the same as that of the dark matter, though this needs to be verified using cosmological simulations.

Our assumption about the efficiency at which gas is converted into stars is necessarily over-simplified, but it is an improvement over the majority of SF recipes (which may be physically or empirically motivated) used in semi-analytic models and hydrodynamical simulations, which are based on the density (or mass) of the total cold gas (atomic plus molecular). We assume an empirical relation between the local star formation rate (SFR) and the local density of molecular gas. We calculate the molecular gas fraction (as a function of radius in the disc) using the empirical relation between midplane pressure and molecular gas fraction from Blitz & Rosolowsky (2006). A more realistic treatment of SF would model the formation and destruction of molecular gas in a physically motivated way (e.g. Pelupessy, Papadopoulos & van der Werf 2006; Robertson & Kravtsov 2008).

In our feedback model, we only consider winds that are able to escape the halo, and assume that mass in such winds is lost forever. In reality mass that escapes the halo may fall back at later times. Furthermore, there may be winds that have enough energy/momentum to escape the disc but not the halo. The gas in these winds could then re-cool back on to the disc producing a galactic fountain. Since very little is known about how feedback works, and our main interest is to determine how much mass can be ejected from the disc and halo rather than introducing additional free parameters to our wind model, we assume the maximal mass-loss model.

The assumption that the halo responds adiabatically to inflows and outflows may not be correct. When galaxies accrete their gas via a smooth cooling flow, the gas radiates away its energy. However, when a galaxy acquires its gas via cold flows, clumps of cold gas can exchange energy with the halo via dynamical friction (e.g. El-Zant, Shlosman & Hoffman 2001; El-Zant et al. 2004; Jardel & Sellwood 2009), causing the halo to expand. In both scenarios, the natural response of the halo to the deepening of the potential well due to the condensation of baryons is to contract, but in the latter scenario, the transfer of energy between baryons and dark matter will counter this effect. Processes internal to discs, such as bars, can also transfer energy to the halo via dynamical friction, causing it to expand (Weinberg & Katz 2002; Holley-Bockelmann, Weinberg & Katz 2005; Sellwood 2008). Mass outflows can also result in halo expansion, e.g. an adiabatic inflow followed by an instantaneous outflow can result in net halo expansion (Navarro, Eke & Frenk 1996; Gnedin & Zhao 2002; Read & Gilmore 2005). Thus, in order to assess how much impact the assumption of adiabatic inflow and outflow has on the structural properties of the resulting galaxies, we also consider models in which the halo does not respond to galaxy formation.

2.2 Dark matter haloes

The backbone of our galaxy formation model is the growth of the dark matter halo, which we model by a smooth MAH. Van den Bosch (2002b) and Wechsler et al. (2002) have shown that the MAH is essentially a one-parameter family. The MAH from Wechsler et al. (2002) is given by

$$M_{\rm vir}(z) = M_{\rm vir}\,\mathrm{e}^{-\alpha z}, \tag{1}$$

where $M_{\rm vir}$ is the redshift zero mass and α is related to the epoch of formation via

$$\alpha = a_{\rm c}\,S. \tag{2}$$

Here, $a_{\rm c} = (1 + z_{\rm c})^{-1}$ is defined as the scalefactor a when the logarithmic slope of the accretion rate falls below some specified value, S. Following Wechsler et al. (2002), we adopt $S = 2$. Before we discuss how to compute $a_{\rm c}$, we discuss how the structural properties of the halo depend on its mass.

In the standard spherical top-hat collapse model, the virial radius, $R_{\rm vir}(z)$, of a halo of mass $M_{\rm vir}(z)$ at a redshift, z, is given by

$$\left[\frac{R_{\rm vir}(z)}{h^{-1}\,\mathrm{kpc}}\right] \simeq 162.6 \left[\frac{M_{\rm vir}(z)}{10^{12}\,h^{-1}\,\mathrm{M}_{\odot}}\right]^{\frac{1}{3}} \left[\frac{200}{\Delta_{\rm vir}(z)}\right]^{\frac{1}{3}} \left[\frac{H_0}{H(z)}\right]^{\frac{2}{3}}, \tag{3}$$

where $h = H_0/100$ and $\Delta_{\rm vir}$ is the virial density, relative to the critical density for closure. We use the fitting formula of Bryan &

Norman (1998)

$$\Delta_{\rm vir} = 18\pi^2 + 82x - 39x^2, \tag{4}$$

with $x = \Omega_{\rm m}(z) - 1$. The evolution of the matter density is given by

$$\Omega_{\rm m}(z) = \Omega_{\rm m,0}(1+z)^3 \left[\frac{H(z)}{H_0}\right]^{-2}, \tag{5}$$

and the evolution of the Hubble parameter is given by

$$H^2(z) = H_0^2\,[\Omega_\Lambda + (1-\Omega_\Lambda - \Omega_{\rm m,0})(1+z)^2 + \Omega_{\rm m,0}(1+z)^3]. \tag{6}$$

The relation between the virial velocity, $V_{\rm vir}$, and virial radius, $R_{\rm vir}$, is given by

$$V_{\rm vir} = \sqrt{\frac{GM_{\rm vir}}{R_{\rm vir}}}. \tag{7}$$

We assume that the density profile of the halo at each redshift is given by an NFW (Navarro, Frenk & White 1997) profile

$$\frac{\rho(R)}{\rho_{\rm crit}} = \frac{\delta_{\rm c}}{(R/R_{\rm s})(1+R/R_{\rm s})^2}, \tag{8}$$

where $R_{\rm s}$ is the radius where the slope of the density profile is -2, the so-called scale radius, $\rho_{\rm crit}$ is the critical density of the universe and $\delta_{\rm c}$ is the characteristic overdensity of the halo. The concentration parameter of the halo is defined as $c = R_{\rm vir}/R_{\rm s}$ and is related to $\delta_{\rm c}$ via

$$\delta_{\rm c} = \frac{\Delta_{\rm vir}}{3}\frac{c^3}{[\ln(1+c) - c/(1+c)]}. \tag{9}$$

Following Bullock et al. (2001a), we assume that the concentration parameter evolves as

$$c(z) = Ka(z)/a_{\rm c} = K\frac{1+z_{\rm c}}{1+z} \tag{10}$$

with a minimum value of $c(z) = K$, corresponding to a constant concentration during the rapid accretion phase of dark halo growth (Zhao et al. 2003). Thus if we specify the redshift zero concentration, we can compute the collapse epoch via $a_{\rm c} = K/c$, and hence the MAH through equations (1) and (2).

To compute the mean concentration for a halo of a given mass at $z = 0$, we use the Bullock et al. (2001a) model. This model requires us to specify the cosmology Ω_Λ, $\Omega_{\rm m,0}$, $\Omega_{\rm b}$, σ_8, n, h, as well as two free parameters, F and K. We assume the concentration is lognormally distributed with median $c(M)$ from the Bullock et al. (2001a) model and scatter $\sigma_{\ln c}$. Our adopted values for these parameters are given in Section 2.10.

2.3 Gas cooling

At each time-step, a shell with mass $\Delta M = M_{\rm vir}(t) - M_{\rm vir}(t-\Delta t)$ virializes. A fraction $f_{\rm bar} = \Omega_{\rm b}/\Omega_{\rm m,0}$ of this mass is in baryons, and is heated to the halo's virial temperature

$$T_{\rm vir} = \frac{1}{2}\frac{\mu\, m_{\rm p}}{k}V_{\rm vir}^2, \tag{11}$$

where $\mu\, m_{\rm p}$ is the mass per particle and k is Boltzmann's constant. The baryons dissipate energy radiatively, lose pressure support and collapse until they reach centrifugal equilibrium. The time-scale over which this occurs is given by $t_{\rm c} \equiv \max[t_{\rm ff}, t_{\rm cool}]$. Here, $t_{\rm ff}$ is the free-fall time defined as

$$t_{\rm ff} = \sqrt{\frac{3\pi}{32G\bar{\rho}}}, \tag{12}$$

with $\bar{\rho}$ as the average halo density, and

$$t_{\rm cool} = \frac{3}{2}\mu m_{\rm p}\frac{kT_{\rm vir}}{\rho_{\rm hot}\Lambda_{\rm N}(Z_{\rm hot})}\frac{\mu_{\rm e}^2}{\mu_{\rm e}-1} \tag{13}$$

is the cooling time. Here, $\rho_{\rm hot}$ is the density of the hot gas, $\mu_{\rm e}$ is the number of particles per electron and $\Lambda_{\rm N}$ is the normalized cooling function for a gas with metallicity $Z_{\rm hot}$. For $\rho_{\rm hot}$, we use $f_{\rm bar}$ times the density at the virial radius at the time the gas enters the halo. For $\Lambda_{\rm N}$, we use the collisional ionization equilibrium cooling functions of Sutherland & Dopita (1993), assuming a helium mass abundance of 0.25.

For each time-step, we compute the range of times between which gas that collapses on to the disc in the current time interval entered the halo. We label these times as $t_{\rm c,min}(t)$ and $t_{\rm c,max}(t)$.

2.4 Angular momentum distribution

The radius at which the cooled gas ends up depends on its specific angular momentum, j. van den Bosch (2001, 2002a) assumed the j-distribution to be that of a shell in solid body rotation. The angular momentum of this shell can be computed assuming that the spin parameter, λ, is constant between time-steps. The spin parameter is defined by

$$\lambda = \frac{J_{\rm vir}|E_{\rm vir}|^{1/2}}{GM_{\rm vir}^{5/2}}, \tag{14}$$

where $M_{\rm vir}$, $J_{\rm vir}$ and $E_{\rm vir}$ are the mass, total angular momentum and energy of the halo, respectively. As shown by van den Bosch (2001), this results in density profiles that are more concentrated than exponential in the centre, and also that truncate at shorter radii than is observed in some disc galaxies.

Building on the work of Bullock et al. (2001b), Sharma & Steinmetz (2005, hereafter SS05) used a series of non-radiative N-body/SPH simulations in a ΛCDM cosmology to study the growth of angular momentum in galaxy systems. They introduced a function that is able to describe, with a single parameter, α, the specific AMD of the gas and dark matter in their simulations, as well as that of exponential discs in NFW haloes:

$$\frac{M(<j)}{M_{\rm vir}} = \gamma(\alpha, \frac{j}{j_{\rm d}}), \quad j_{\rm d} = \frac{J_{\rm vir}}{M_{\rm vir}}\frac{1}{\alpha}, \tag{15}$$

where γ is the incomplete gamma function. SS05 found that the distribution of α is lognormally distributed with mean $\log\alpha \simeq -0.05$ and standard deviation in $\log\alpha \simeq 0.11$.

In summary, the distribution of specific angular momentum of the dark matter halo and hot gas can be described by two parameters: a normalization (λ) and a shape (α). Both the normalization and shape parameters are lognormally distributed, with significant scatter. We assume that the spin and shape parameters are uncorrelated, although Bullock et al. (2001b) show that there may be a weak correlation between λ and α. Furthermore, we assume that, for a given halo, λ and α are constant with redshift. These assumptions are made for simplicity, and need to be tested with cosmological simulations.

In order to compute the amount of mass, with a given specific angular momentum, j, that has collapsed on to the disc in each time-step, $M_{\rm c}$, we take the difference between the distributions of specific angular momentum of the haloes at times $t_{\rm c,min}$ and $t_{\rm c,max}$ ($t_{\rm c,min}$ and $t_{\rm c,max}$ are defined in Section 2.3 above):

$$M_{\rm c}(<j)(t) = f_{\rm bar}[M_{\rm vir}(<j)(t_{\rm c,max}) - M_{\rm vir}(<j)(t_{\rm c,min})]. \tag{16}$$

2.5 Conservation of angular momentum and halo contraction

In order to compute the radius, R, at which material with specific angular momentum, j, ends up, we assume that specific angular momentum is conserved, i.e. one should solve

$$j = R\,V_{\rm circ}(R) \tag{17}$$

for R. Here, $V_{\rm circ}$ is the total circular velocity (from stars, cold gas, hot gas and dark matter).

As the galaxy grows over time, the circular velocity at a given radius increases. Thus to conserve specific angular momentum, material that settled at radius R would need to drift to smaller radii over time. Given that the gas and stars effect the circular velocity, strictly conserving the specific angular momentum of the baryons over time is difficult to implement numerically. To get around this problem, we use specific angular momentum, j, rather than radius as our radial coordinate.

Under the simplifying assumption that $V_{\rm circ} = [GM(<R)/R]^{1/2}$, where $M(<R)$ is the total mass within a spherical radius, R, the radius that corresponds to a given j is given by

$$R = \frac{j^2}{GM(<j)}. \tag{18}$$

This has a number of desirable properties: (1) at each time-step, it is trivial to calculate how much cold gas is added to each bin in j; (2) over time, as the potential well changes, the specific angular momentum of the baryons is automatically conserved; (3) the response of the halo to the cooling of the baryons is automatically taken into account and (4) the resulting radial grid is adaptive, as the mapping between j and R depends on the amount of mass enclosed.

The price that we pay for these advantages is that the circular velocity due to the disc is not calculated correctly. Due to the disc geometry, the true circular velocity deviates from that given by the spherically enclosed mass. For example, the peak $V_{\rm circ}$ of a thick exponential disc is $\simeq$10 per cent higher than that obtained using the enclosed mass, and at small radii the proper $V_{\rm circ}$ increases linearly with radius, whereas using the enclosed mass $V_{\rm circ}$ scales as $R^{1/2}$.

However, given that computing the proper circular velocity of the disc is very time consuming, that it is sensitive to gradients in the disc density profile and that using it would remove the simplicity of the j-grid approach, we feel that it is a price worth paying.

As we show below (in Section 3), and as discussed in D07, models with halo contraction [and standard stellar initial mass functions (IMFs)] are unable to reproduce the zero-points of the *VMR* relations as well as the low galaxy formation efficiency required to reconcile the halo mass function and galaxy stellar mass function. While there are processes such as dynamical friction and impulsive mass loss that can expand the halo, implementing these in a galaxy evolution model is a non-trivial task. Thus for simplicity we wish to consider a model in which the dark halo does not respond to galaxy formation.

Note that simply using the mapping between radius and j based on the halo profile (at each time-step) in the absence of galaxy formation would not conserve the specific angular momentum of the baryons. To calculate the mapping between j and radius, for the case of *no adiabatic contraction*, we solve the equation

$$R = \frac{j^2/G}{M_{\rm halo}(<R) + M_{\rm disc}(<j)}, \tag{19}$$

where $M_{\rm halo}(R)$ is the mass (within a spherical radius R) of the dark matter plus hot gas halo in the absence of galaxy formation and $M_{\rm disc}(j)$ is the mass of the disc (gas plus stars) with specific angular momentum less than j. This way the self-gravity of the disc is included but adiabatic contraction is ignored.

2.6 Star formation

Observations have shown that the disc-averaged SFRs in nearby spiral galaxies are well fitted by a simple Schmidt (1959) law

$$\frac{\Sigma_{\rm SFR}}{({\rm M_\odot\,pc^{-2}\,Gyr^{-1}})} = \frac{\epsilon_{\rm SF}}{({\rm M_\odot\,pc^{-2}\,Gyr^{-1}})}\left[\frac{\Sigma_{\rm gas}}{(1\,{\rm M_\odot\,pc^2})}\right]^n. \tag{20}$$

Kennicutt (1998) used $\Sigma_{\rm gas}$ as the total gas density (molecular and atomic, but not including helium) and found $\epsilon_{\rm SF} = 0.25\,{\rm M_\odot\,pc^{-2}\,Gyr^{-1}}$ and $n = 1.4 \pm 0.15$ (Kennicutt 1998).[1] This simple empirical law holds over many orders of magnitude in gas surface density, and even applies to circumnuclear starburst regions. However, when applied to local gas densities, the Schmidt law breaks down at low gas densities, corresponding to large radii, where SF has been found to be abruptly suppressed. Kennicutt (1989) argued that this suppression is due to the gas density falling below the critical density for global disc stability as given by the Toomre criterion (Toomre 1964)

$$\Sigma_{\rm crit} = \sigma_{\rm gas}\kappa(R)/3.36GQ, \tag{21}$$

where $\sigma_{\rm gas}$ is the velocity dispersion of the gas, κ is the epicyclic frequency and Q is the Toomre Q parameter. Kennicutt (1989) found that $\sigma_{\rm gas} = 6\,{\rm km\,s^{-1}}$ and $Q = 1.5$ reproduce the observed SF truncation radii. However, other authors argue that this is just a coincidence, and that $\Sigma_{\rm crit}$ is not a threshold density (e.g. Schaye 2004).

The physical origin of the Schmidt–Kennicutt (SK) relation is also not clear. However, something that is well established is that stars form out of molecular gas, and predominantly in giant molecular clouds. This leads Wong & Blitz (2002) to argue for a Schmidt law based on the surface density of molecular gas. For high gas densities, the molecular gas dominates, so the two prescriptions are identical. However, for low gas densities the molecular fraction is suppressed, resulting in a steep dependence of the SFR density on total gas density. This gives an alternative explanation for the suppression of SF at low gas densities.

The fraction of gas that is molecular, $f_{\rm mol}$, can be defined in terms of the mass ratio between molecular and atomic gas, $\mathcal{R}_{\rm mol}$, by

$$f_{\rm mol} = \frac{\mathcal{R}_{\rm mol}}{\mathcal{R}_{\rm mol}+1}. \tag{22}$$

Empirically, Wong & Blitz (2002) and Blitz & Rosolowsky (2004, 2006) have argued that $\mathcal{R}_{\rm mol}$ is determined to first order by the mid-plane pressure, $P_{\rm ext}$. The most recent relation from Blitz & Rosolowsky (2006) is

$$\mathcal{R}_{\rm mol} = \frac{\Sigma_{\rm mol}}{\Sigma_{\rm atom}} = \left(\frac{P_{\rm ext}/k}{4.3 \pm 0.6 \times 10^4}\right)^{0.92\pm0.1}, \tag{23}$$

where k is Boltzmann's constant and $P_{\rm ext}/k$ is in cgs units. For a gas plus stellar disc, the mid-plane pressure is given to within 10 per cent by (Elmegreen 1993)

$$P_{\rm ext} \simeq \frac{\pi}{2}G\Sigma_{\rm gas}\left[\Sigma_{\rm gas} + \left(\frac{\sigma_{\rm gas}}{\sigma_{\rm star}}\right)\Sigma_{\rm star}\right], \tag{24}$$

where $\sigma_{\rm gas}$ and $\sigma_{\rm star}$ are the velocity dispersions of the gas and stellar disc, respectively. For simplicity, we will assume $\sigma_{\rm gas}/\sigma_{\rm star} = 0.1$ which is a reasonable assumption for the stellar-dominated parts of disc galaxies. In the outer parts of disc galaxies, this ratio is likely to be higher. However, in these regions gas dominates, and so the

[1] Including a helium correction of 1.36 results in $\epsilon_{\rm SF} = 0.16\,{\rm M_\odot\,pc^{-2}\,Gyr^{-1}}$.

contribution of the stars to the mid-plane pressure is negligible, regardless of the ratio between $\sigma_{\rm gas}$ and $\sigma_{\rm star}$. In the inner regions of galaxies, $\sigma_{\rm gas}/\sigma_{\rm star}$ is likely to be smaller than 0.1, but here the densities are high enough that $f_{\rm mol} \simeq 1$.

Following Blitz & Rosolowsky (2006), we assume that SF takes place in dense molecular gas, traced by HCN, with a constant SF efficiency

$$\frac{\Sigma_{\rm SFR}}{({\rm M_\odot\,pc^{-2}Gyr^{-1}})} = \frac{\tilde{\epsilon}_{\rm SF}}{({\rm Gyr^{-1}})}\,\frac{\Sigma_{\rm mol,HCN}}{({\rm M_\odot\,pc^{-2}})}, \tag{25}$$

where $\tilde{\epsilon}_{\rm SF} \simeq 10{-}13\,{\rm Gyr^{-1}}$ (Gao & Solomon 2004, Wu et al. 2005). Expressing this equation in terms of the total gas content:

$$\frac{\Sigma_{\rm SFR}}{({\rm M_\odot\,pc^{-2}\,Gyr^{-1}})} = \frac{\tilde{\epsilon}_{\rm SF}}{({\rm Gyr^{-1}})}\,\frac{\Sigma_{\rm gas}}{({\rm M_\odot\,pc^{-2}})}\,f_{\rm mol}\,\mathcal{R}_{\rm HCN}, \tag{26}$$

where $\mathcal{R}_{\rm HCN} = \Sigma_{\rm mol,HCN}/\Sigma_{\rm mol}$ is the ratio between the dense molecular gas (as traced by HCN) and the total molecular gas.

Based on the arguments and references in Blitz & Rosolowsky (2006), we adopt the following relation for $\mathcal{R}_{\rm HCN}$:

$$\mathcal{R}_{\rm HCN} = 0.1\left[1 + \frac{\Sigma_{\rm mol}}{(200\,{\rm M_\odot\,pc^{-2}})}\right]^{0.4}. \tag{27}$$

In the low-pressure, low-molecular-density regime, $\mathcal{R}_{\rm HCN} \simeq 0.1$, and thus equation (25) asymptotes to

$$\frac{\Sigma_{\rm SFR}}{({\rm M_\odot\,pc^{-2}\,Gyr^{-1}})} = \frac{\tilde{\epsilon}_{\rm SF}}{({\rm Gyr^{-1}})}\,\frac{0.013}{({\rm M_\odot\,pc^{-2}})}\left[\frac{\Sigma_{\rm gas}}{({\rm M_\odot\,pc^{-2}})}\right]^{2.84}. \tag{28}$$

In the high-pressure, high-molecular-density regime, $\mathcal{R}_{\rm HCN} \propto \Sigma_{\rm mol}^{0.4}$, and equation (25) asymptotes to the familiar SK relation

$$\frac{\Sigma_{\rm SFR}}{({\rm M_\odot\,pc^{-2}\,Gyr^{-1}})} = \frac{\tilde{\epsilon}_{\rm SF}}{({\rm Gyr^{-1}})}\,\frac{0.012}{({\rm M_\odot\,pc^{-2}})}\left[\frac{\Sigma_{\rm gas}}{({\rm M_\odot\,pc^{-2}})}\right]^{1.4}. \tag{29}$$

Furthermore, with $\tilde{\epsilon}_{\rm SF} = 13\,{\rm Gyr^{-1}}$, we recover the coefficient of $\epsilon_{\rm SF} = 0.16$ of the standard SK relation.

Fig. 1 shows the relation between SFR density and gas density for our SF model (equation 25). Note that in order to compute $\Sigma_{\rm SFR}$ one needs to know $\Sigma_{\rm star}$ and $\Sigma_{\rm gas}$. For illustrative purposes, we have chosen a stellar and gas density profile representative of bright nearby disc galaxies (left-hand panel of Fig. 1). At small radii and high gas densities $f_{\rm mol} \simeq 1$, and the SF law follows the standard SK relation. At large radii, the molecular fraction is very low, which results in a steeper slope to the SF law.

We implement the SF recipe given by equation (25) as follows. At each time-step and annulus in the disc, we calculate the SFR. Then, we use the following approximation (valid for time-steps small compared to the SF time-scale) to calculate the mass of newly formed stars

$$\Delta M_{\rm star}(R) = A(R)\,\Sigma_{\rm SFR}(R,t)\,\Delta t, \tag{30}$$

with A as the area of the annulus and Δt the time-step interval.

2.7 Supernova feedback

When stars evolve they put energy back into the interstellar medium (ISM). The effect of this on the SFR is partially taken into account by our empirically determined SF recipe. What is not taken into account is a feedback-driven outflow of gas from the disc. The physical mechanism responsible for driving outflows is a subject of debate (e.g. Finlator & Davé 2008), so in this paper we consider both energy- and momentum-driven winds.

Following van den Bosch (2001), we assume that the outflow moves at the local escape velocity of the disc–halo system. This choice is motivated by the fact that it maximizes the mass loss from the disc–halo system (lower velocity winds will not escape the halo, and higher velocity winds will carry less mass).

For our energy-driven wind model, following Dekel & Silk (1986), we assume that the kinetic energy of the wind is equal to a fraction, $\epsilon_{\rm EFB}$, of the kinetic energy produced by SN. However, contrary to Dekel & Silk (1986), we apply this energy condition *locally* in the disc as a function of radius, rather than globally to the whole galaxy. Thus the mass ejected from radius, R, during a given time-step is given by

$$\Delta M_{\rm eject}(R) = \frac{2\,\epsilon_{\rm EFB}\,E_{\rm SN}\,\eta_{\rm SN}}{V_{\rm esc}^2(R)}\,\Delta M_{\rm star}(R). \tag{31}$$

Here, $\Delta M_{\rm star}(R)$ is the mass in stars formed at radius, R, $E_{\rm SN} = 10^{51}\,{\rm erg} \simeq 5.0\times10^7\,{\rm km^2\,s^{-2}\,M_\odot}$ is the energy produced by one SN and $\eta_{\rm SN} = 8.3\times10^{-3}$ is the number of SN per solar mass of stars formed (for a Chabrier IMF).

The local escape velocity is given by

$$V_{\rm esc}(R) = \sqrt{2|\Phi_{\rm tot}(R)|}, \tag{32}$$

where $\Phi_{\rm tot}$ is the sum of the potentials due to the disc (stars plus gas) and halo (dark matter plus hot gas) and is computed assuming spherical symmetry.

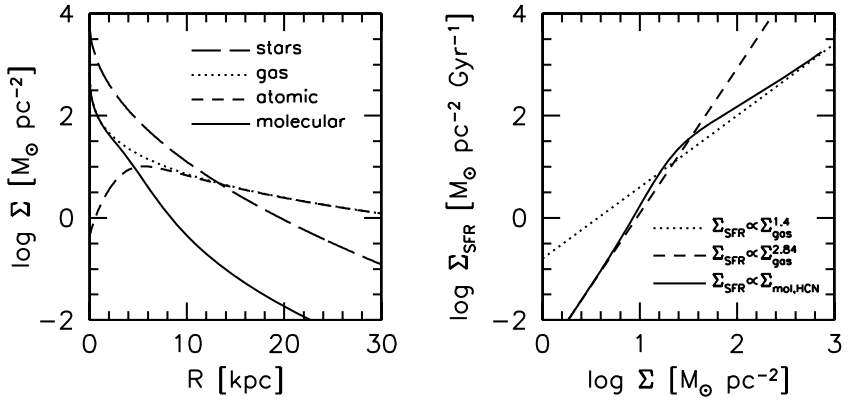

Figure 1. Right-hand panel: SF surface density versus total gas surface density for our adopted SF model (equation 25), with $\tilde{\epsilon}_{\rm SF} = 13\,{\rm Gyr^{-1}}$. This has been calculated using the molecular and total gas densities of the model in the left-hand panel. The dotted line shows the standard SK relation, which our model converges to at high gas density (equation 29). The dashed line shows the relation our model converges to at low gas density (equation 28). Left-hand panel: surface density profiles of stars and gas (total, atomic and molecular) which is used to calculate the right-hand panel. The molecular fraction is computed using equations (22)–(24).

For our momentum-driven wind model, we assume that the momentum of the wind is equal to a fraction, $\epsilon_{\rm MFB}$, of the momentum produced by SN, thus the mass ejected from radius, R, during a given time-step is given by

$$\Delta M_{\rm eject}(R) = \frac{\epsilon_{\rm MFB}\, p_{\rm SN}\, \eta_{\rm SN}}{V_{\rm esc}(R)} \Delta M_{\rm star}(R). \quad (33)$$

Here, $p_{\rm SN} = 3 \times 10^4\,{\rm M}_\odot\,{\rm km\,s^{-1}}$ is the momentum produced by one SN, assuming that each SN produces $\simeq$10 $\rm M_\odot$ of material moving at $v \simeq 3000\,{\rm km\,s^{-1}}$ (Murray, Quataert & Thompson 2005). Note that this corresponds to a kinetic energy of $4.5 \times 10^7\,{\rm M_\odot\,km^2\,s^{-2}} \simeq 10^{51}$ erg.

We assume that the ejected mass is lost forever from the system: the ejected mass is not considered for later infall, and the corresponding metals are not used to enrich the infalling gas. This is clearly a dramatic oversimplification, but we make this choice to maximize the amount of gas that is lost from the system.

2.8 Stellar populations and chemical enrichment

In order to convert stellar mass into luminosities, we use the Bruzual & Charlot (2003) stellar population synthesis models. These models provide the luminosities $L(t, Z)$ of a single burst stellar population with a total mass of $1\,{\rm M_\odot}$ as a function of age, t, and metallicity, Z, in various optical passbands. To compute the luminosities of our model stellar populations, we convolve the SF history of our galaxies with the single burst stellar population synthesis models.

In order to model the chemical enrichment of the ISM, we adopt the instantaneous recycling approximation. We assume that a fraction $\mathcal{R}$ of the mass in stars formed is instantaneously returned to the cold gas phase with a yield y (defined as the fraction of mass converted into stars that is returned to the ISM in the form of newly processed metals).

The equations for the change in the cold gas mass and metals are

$$\Delta M_{\rm cold} = \Delta M_{\rm cool} - (1 - \mathcal{R})\Delta M_{\rm star} - \Delta M_{\rm eject}, \quad (34)$$

$$\Delta M_{\rm metal} = Z_{\rm hot}\,\Delta M_{\rm cool} - Z_{\rm cold}(1 - \mathcal{R})\Delta M_{\rm star} + y\Delta M_{\rm star} - Z_{\rm cold}\Delta M_{\rm eject}. \quad (35)$$

The metallicity of the cold gas is then given by $Z_{\rm cold} = M_{\rm metal}/M_{\rm cold}$. Note we assume that the ejected metals do not enrich the hot halo gas.

2.9 Book keeping

We now briefly describe how we keep track of the evolution of the various mass components. Given a $z = 0$ halo mass (dark matter plus hot gas) and concentration, we compute the MAH of the halo using equation (1). The evolution of the virial radius and internal structure of the halo is then determined by equations (3) and (10). We set up a grid in radius from 0.001 to 1 times the redshift zero virial radius. As described in Section 2.5, for the purposes of conserving angular momentum it is more convenient to use a grid in specific angular momentum, j. Thus we convert the grid in R to a grid in j using $j^2/G = RM(R)$.

For each time-step $(t - \Delta t, t)$, we compute the halo mass that is added to each radial bin so that the total mass follows the NFW profile for a halo of a given $c(z)$ and $M_{\rm vir}(z)$. Thus,

$$\Delta M_{\rm vir}(j, t) = M_{\rm vir}(j, t) - M_{\rm vir}(j, t - \Delta t). \quad (36)$$

We assume that the baryons make up a fraction $f_{\rm bar}$ of this mass, so that

$$\Delta M_{\rm DM}(j, t) = (1 - f_{\rm bar})\Delta M_{\rm vir}(j, t), \quad (37)$$

$$\Delta M_{\rm hot}(j, t) = f_{\rm bar}\Delta M_{\rm vir}(j, t). \quad (38)$$

When we compute the circular velocity, we assume that the hot gas follows the mass distribution of the dark matter. When computing the cooling time we assume $\rho_{\rm hot}$ is $f_{\rm bar}$ times the density at the virial radius at the time when the gas virialized.

At each time-step, we then compute, using the recipes in the previous sections, the amount of gas that cools, $\Delta M_{\rm cool}(j, t)$, the amount of stars formed $\Delta M_{\rm star}(j, t)$, and the amount of ejected gas $\Delta M_{\rm eject}(j, t)$. For the stellar population modelling, we keep track of the mass of stars formed at each time-step and the metallicity of the gas from which the stars formed, $Z_{\rm cold}(j, t)$.

2.10 Overview of model parameters

The input parameters of our models are as follows.

(1) Cosmology: $\Omega_{\rm m,0}$, Ω_Λ, $\Omega_{\rm b}$, σ_8, h, n. In this paper, we adopt a flat ΛCDM cosmology motivated by the fifth-year *Wilkinson Microwave Anisotropy Probe* (*WMAP*) results (Dunkley et al. 2009), with $\Omega_{\rm m,0} = 0.258$, $\Omega_\Lambda = 0.742$, $\Omega_{\rm b} = 0.044, h = 0.7, \sigma_8 = 0.80$ and $n = 1$.

(2) Halo structure: $K, F, \sigma_{\ln c}$. We adopt the Bullock et al. (2001a) model with $F = 0.01$, $K = 3.7$ and $\sigma_{\ln c} = 0.25$. These parameters reproduce the distribution of halo concentrations of relaxed dark matter haloes in numerical simulations (Wechsler et al. 2002; Macciò et al. 2007; Macciò, Dutton & van den Bosch 2008).

(3) AMD: $\bar{\lambda}$, $\sigma_{\ln\lambda}$, α, $\sigma_{\log\alpha}$. As fiducial values, we adopt a median spin parameter $\bar{\lambda} = 0.035$ with a scatter $\sigma_{\ln\lambda} = 0.54$, corresponding to relaxed haloes (Macciò et al. 2007, 2008). For the angular momentum shape parameter, we adopt a median $\bar{\alpha} = 0.90$ and scatter $\sigma_{\log\alpha} = 0.11$ (SS05).

(4) SF: $\tilde{\epsilon}_{\rm SF}$. We use a SF model based on dense molecular gas (equation 25), and adopt $\tilde{\epsilon}_{\rm SF} = 13\,{\rm Gyr^{-1}}$.

(5) Feedback: $\epsilon_{\rm EFB}$, $\epsilon_{\rm MFB}$, $\eta_{\rm SN}$, $E_{\rm SN}$, $p_{\rm SN}$. We adopt $E_{\rm SN} = 10^{51}$ erg, $p_{\rm SN} = 3 \times 10^4\,{\rm M_\odot\,km\,s^{-1}}$, $\eta_{\rm SN} = 8.3 \times 10^{-3}$. We treat $\epsilon_{\rm EFB}$ and $\epsilon_{\rm MFB}$ as free parameters.

(6) Stellar populations and chemical enrichment: $\mathcal{R}$, y, $Z_{\rm hot}$ and the choice of IMF. We adopt the Chabrier (2003) IMF, a return fraction $\mathcal{R} = 0.35$, a stellar yield $y = 0.02$ and a metallicity of the hot gas of $Z_{\rm hot} = 0.002$ ($\simeq$0.1 $\rm Z_\odot$).

2.11 Overview of output parameters

The output parameters of our models, that we discuss in this paper, are as follows.

(i) $M_{\rm vir}$, total mass inside virial radius ($\rm M_\odot$).
(ii) $V_{\rm vir}$, circular velocity at the virial radius ($\rm km\,s^{-1}$).
(iii) $V_{\rm max,h}$, maximum circular velocity of the halo without galaxy formation ($\rm km\,s^{-1}$).
(iv) $M_{\rm gal}$, galaxy mass (stars and cold gas) ($\rm M_\odot$).
(v) $M_{\rm star}$, stellar mass ($\rm M_\odot$).
(vi) $M_{\rm cold}$, cold gas mass ($\rm M_\odot$).
(vii) $Z_{\rm cold}$, metallicity of cold gas.
(viii) $\epsilon_{\rm GF} = m_{\rm gal}/(\Omega_{\rm b}/\Omega_{\rm m,0})$, galaxy formation efficiency.
(ix) $m_{\rm gal} = M_{\rm gal}/M_{\rm vir}$, galaxy mass fraction.
(x) $m_{\rm star} = M_{\rm star}/M_{\rm vir}$, stellar mass fraction.
(xi) $m_{\rm cold} = M_{\rm cold}/M_{\rm vir}$, cold gas mass fraction.

(xii) $f_{\rm gas} = M_{\rm cold}/(M_{\rm cold} + M_{\rm star})$, cold gas fraction.

(xiii) $V_{2.2I}$, the circular velocity measured at 2.15 I-band disc scalelengths (km s^{-1}).

(xiv) $R_{{\rm d}I}$, I-band disc scalelength (kpc).

(xv) $j_{\rm gal} = J_{\rm gal}/J_{\rm vir}$, galaxy angular momentum fraction.

(xvi) $j_{\rm star} = J_{\rm star}/J_{\rm vir}$, stellar angular momentum fraction.

(xvii) $j_{\rm cold} = J_{\rm cold}/J_{\rm vir}$, cold gas angular momentum fraction.

(xviii) $\lambda_{\rm gal} = \lambda\ (j_{\rm gal}/m_{\rm gal})$, galaxy spin parameter.

(xix) $\lambda_{\rm star} = \lambda\ (j_{\rm star}/m_{\rm star})$, stellar spin parameter.

(xx) $\lambda_{\rm cold} = \lambda\ (j_{\rm cold}/m_{\rm cold})$, cold gas spin parameter.

(xxi) $\dot{M}_{\rm bar} = f_{\rm bar}\dot{M}_{\rm vir}$, the baryonic mass accretion rate (M$_\odot$ Gyr^{-1}).

(xxii) $\dot{M}_{\rm cool}$, the mass cooling rate (M$_\odot$ Gyr^{-1}).

(xxiii) $\dot{M}_{\rm SF}$, the SFR (M$_\odot$ Gyr^{-1}).

(xxiv) $\dot{M}_{\rm w}$, the mass outflow rate (M$_\odot$ Gyr^{-1}).

(xxv) $\eta = \dot{M}_{\rm w}/\dot{M}_{\rm sf}$, the mass loading factor.

(xxvi) $V_{\rm w} = \Sigma_i V_{\rm w}(i)\dot{M}_{\rm w}(i)/\dot{M}_{\rm w}$, the (outflow) mass-weighted mean outflow velocity (km s^{-1}), where i refers to the radial grid position.

The disc scalelengths are determined using the following procedure, which was developed to give robust disc scalelengths for the full range of surface brightness profiles produced by our model. We first compute the local disc scalelength between the radii enclosing 50 and 99 per cent of the stellar mass. The local disc scalelength is computed at radial bin i by using the surface densities and radii at radial bins $i - 1$ and $i + 1$. We then determine the maximum of the local disc scalelength and the radius where this maximum occurs, $R_{\rm max}$. Finally, we determine the scalelength of the disc using a linear fit to the model data over the range $0.6R_{\rm max} \leq R \leq 1.6\ R_{\rm max}$.

2.12 Comparison with other disc galaxy structure models

In this section, we place our model in the context of existing analytic and semi-analytic models of disc galaxy structure/formation in the literature. We classify these models into two general types: (1) models that conserve *total* specific angular momentum (i.e. the structural profile of the disc is assumed) and (2) models that conserve the *distribution* of specific angular momentum (i.e. the structural profile of the disc is derived). Both of these classes of models can be static or include evolution. The essential assumption in both classes of models is that the disc is in centrifugal equilibrium inside some potential (which may or may not include the self-gravity of the disc).

2.12.1 Models that conserve total specific angular momentum

In the simplest models of this class, the circular velocity is assumed to be constant, i.e. corresponding to an isothermal density profile, and the self-gravity of the disc is ignored. This model has three parameters: the circular velocity, the spin parameter and the disc mass fraction. Such a model was discussed in MMW, and is widely used in semi-analytic models (e.g. Kauffmann, White & Guiderdoni 1993; Cole et al. 1994; Somerville & Primack 1999; Hatton et al. 2003; Croton et al. 2006).

A more realistic version of this model includes the self-gravity of the disc and adiabatic contraction of the halo (Blumenthal et al. 1986), which usually results in smaller sizes for a given spin parameter and disc mass fraction. In MMW, the halo was assumed to be an NFW profile, and the disc was assumed to be exponential. This model has four parameters: the circular velocity of the halo, the concentration of the halo, the spin parameter and the disc mass fraction. This version of the MMW model is widely used in semi-analytic models (Cole et al. 2000; Benson et al. 2003; Somerville et al. 2008) and studies of disc galaxy scaling relations (e.g.Navarro & Steinmetz 2000; Pizagno et al. 2005; D07; Gnedin et al. 2007).

2.12.2 Models that conserve the distribution of specific angular momentum

The MMW-type model is useful for understanding the origin of disc galaxy scaling relations, but it does not explain the origin of the density profiles of galaxy discs or the relation between gas and stars in galaxy discs. In order to address these questions, one needs to start from some specific AMD. This AMD may be that of a sphere in solid body rotation, or preferably that found in cosmological simulations (e.g. Bullock et al. 2001b). The radial density profile of the disc is then determined by detailed conservation of specific angular momentum.

As with the MMW-type models, these models may ignore the self-gravity of the disc by assuming that the total density profile is isothermal (e.g. Ferguson & Clarke 2001), or include the self-gravity of he disc inside a dark matter halo (e.g. Dalcanton, Spergel & Summers 1997). These models may also include evolution of the baryonic disc, by following the cooling of gas inside growing dark mater haloes, and evolution of the stellar disc, by following the SF as a function of radius (e.g. Firmani & Avila-Reese 2000a; van den Bosch 2001, 2002a; Stringer & Benson 2007).

Our model falls into this latter category, being an evolution of the van den Bosch (2001, 2002a) models. The strength of these models over the MMW-type models is that they can be used to self-consistently study the origin and evolution of disc density profiles (stars, gas, SFRs, inflows, outflows, metallicity, stellar ages) and rotation curve shapes.

3 THE DEPENDENCE OF THE GALAXY VELOCITY–MASS–SIZE RELATIONS ON FEEDBACK

In this section, we investigate the dependence of the scaling relations among rotation velocity, stellar mass and stellar disc scale size on the feedback model.

3.1 Observed disc galaxy scaling relations

Here, we overview the main observed velocity, mass, size and scaling relations that we are going to compare our models to. We use the relations between rotation velocity at 2.2 I-band disc scalelengths, $V_{2.2I}$, stellar mass, $M_{\rm star}$, and I-band disc scalelength, $R_{{\rm d}I}$, from the data set of Courteau et al. (2007), as presented in D07. The stellar masses in D07 were derived from I-band luminosities using the relations from Bell et al. (2003) corresponding to a diet Salpeter IMF. Here, we adopt a Chabrier IMF, and so subtract 0.10 dex from the stellar masses.

The stellar mass TF relation is given by

$$\log \frac{V_{2.2I}}{({\rm km\,s^{-1}})} = 2.195 + 0.259 \left[\log \frac{M_{\rm star}}{(h_{70}^{-2}\,{\rm M}_\odot)} - 10.5\right], \qquad (39)$$

the size–stellar-mass relation is given by

$$\log \frac{R_{{\rm d}I}}{(h_{70}^{-1}\,{\rm kpc})} = 0.491 + 0.281 \left[\log \frac{M_{\rm star}}{(h_{70}^{-2}\,{\rm M}_\odot)} - 10.5\right] \qquad (40)$$

and the corresponding size–velocity relation is given by

$$\log \frac{R_{dI}}{(h_{70}^{-1}\,\mathrm{kpc})} = 0.491 + 1.086 \left[\log \frac{V_{2.2I}}{(\mathrm{km\,s^{-1}})} - 2.195\right]. \quad (41)$$

The intrinsic scatter in these relations is estimated to be $\sigma_{\log_{10} V|M} \simeq 0.05$, $\sigma_{\log_{10} R|M} \simeq 0.13$ and $\sigma_{\log_{10} R|V} \simeq 0.16$. The errors on the slopes of the *VM*, *RM* and *RV* relations from fitting uncertainties are 0.01, 0.02 and 0.12, respectively. However, systematic uncertainties are significantly larger, and harder to quantify. The most significant selection effect for the slope of the *RM* relation is surface brightness. The data set compiled by Courteau et al. (2007) is likely missing lower surface brightness galaxies, and thus overestimates the slope of the size–mass relation at low masses. Such a conclusion is supported by Shen et al. (2003) who studied the half-light radius–stellar-mass relation ($R_{50} - M_{\rm star}$) for a much larger sample of galaxies ($\sim 10^5$) from the Sloan Digital Sky Survey. They find a log slope of 0.14 at low masses, increasing to 0.39 at high masses.

3.2 A fiducial model

To illustrate the effect that feedback has on observable properties of disc galaxies, we consider a model with virial mass $M_{\rm vir} = 6.3 \times 10^{11}\,h^{-1}\,\mathrm{M}_\odot$, and median concentration and angular momentum parameters: $c_{\rm vir} = 9.9$, $\lambda = 0.035$ and $\alpha = 0.9$. The results of varying the energy and momentum feedback efficiency parameters from 0 to 1 are shown in Figs 2 and 3, respectively. The main panels show the *VMR* relations with the solid line showing the mean relations from observations and the dashed lines showing the 2σ scatter. The upper-right panels in these figures show the more theoretical parameters $m_{\rm gal}$ and $\lambda_{\rm gal}$. These are not directly observable because they require knowledge of the halo mass, a quantity that cannot, at present, be reliably measured for individual galaxies.

We first focus on the models with energy feedback and adiabatic contraction (solid red points and lines in Fig. 2). A model with no feedback ($\epsilon_{\rm EFB} = 0$) results in a galaxy mass fraction of $\simeq 0.8\,f_{\rm bar}$ (where $f_{\rm bar} \simeq 0.17$ is the universal baryon fraction). The galaxy formation efficiency is less than 1 because cooling starts to become inefficient at late times. Since the highest specific angular momentum material is accreted last, and this does not have time to cool, the spin of the galaxy is slightly lower than that of the halo. The high galaxy formation efficiency results in a disc scalelength a factor of $\simeq 1.8$ too small and a circular velocity at 2.2 disc scalelengths a factor of $\simeq 1.5$ too high.

When feedback is included, some of the cold baryons are ejected from the disc (and halo). This trivially results in lower $m_{\rm gal}$ (hence lower baryonic mass) but also, non-trivially, higher $\lambda_{\rm gal}$. The higher $\lambda_{\rm gal}$ is due to the preferential ejection of low-angular-momentum material, which we discuss in more detail in Section 4. Both of these effects result in larger, lower surface density discs, which

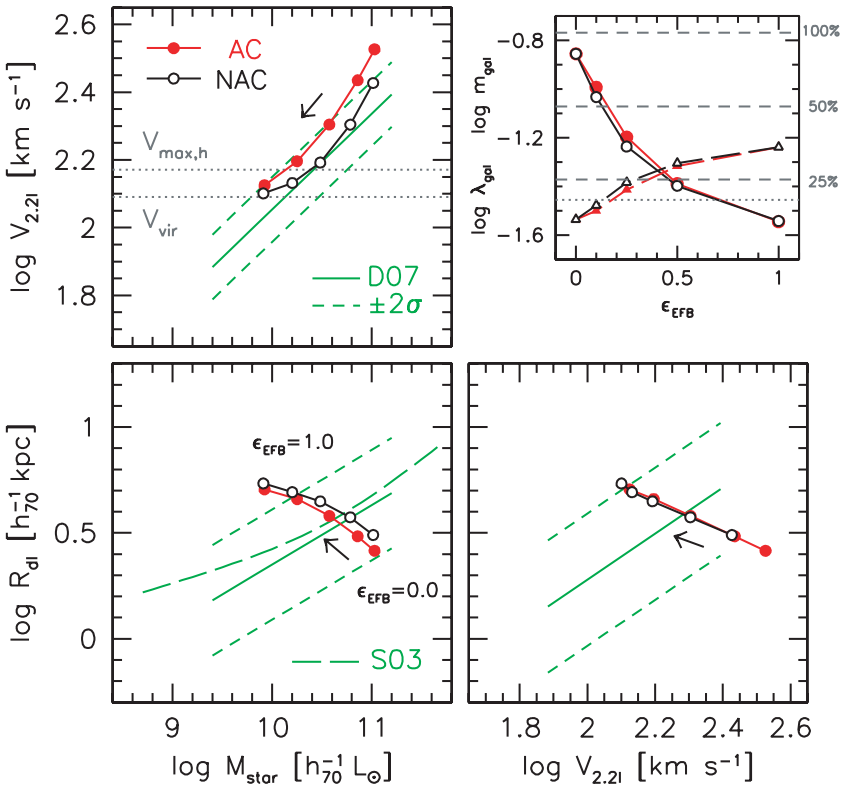

Figure 2. Effect of energy feedback efficiency, $\epsilon_{\rm EFB}$, on the position of a galaxy with $M_{\rm vir} = 6.3 \times 10^{11}\,h^{-1}\,\mathrm{M}_\odot$ in the *VMR* planes. Models have feedback efficiencies of $\epsilon_{\rm EFB} = 0$, 0.1, 0.25, 0.5 and 1.0. The arrows indicate the direction of increasing $\epsilon_{\rm EFB}$. Models with adiabatic contraction are shown with solid red symbols, models without adiabatic contraction are shown as black open symbols. In the *VM* plane, the horizontal dotted grey lines show virial velocity of the halo, $V_{\rm vir}$, and the maximum circular velocity of the halo prior to galaxy formation, $V_{\rm max,h}$. The solid and dashed green lines in the *VMR* panels show the mean and 2σ scatter of the observed relations from D07, assuming a Chabrier IMF. The long dashed green line shows the observed half-light radius–stellar-mass relation from Shen et al. (2003). The panel in the top right shows the effect of feedback on the galaxy mass fraction, $m_{\rm gal}$ (circles), and galaxy spin parameter, $\lambda_{\rm gal}$ (triangles). The dashed horizontal lines show galaxy formation efficiencies of 100, 50 and 25 per cent, the dotted horizontal line shows the spin parameter of the halo. As the feedback efficiency is increased, the galaxy mass fraction ($m_{\rm gal}$) decreases, the galaxy spin parameter ($\lambda_{\rm gal}$) increases, the rotation velocity decreases, the stellar mass decreases and the size of the stellar disc increases.

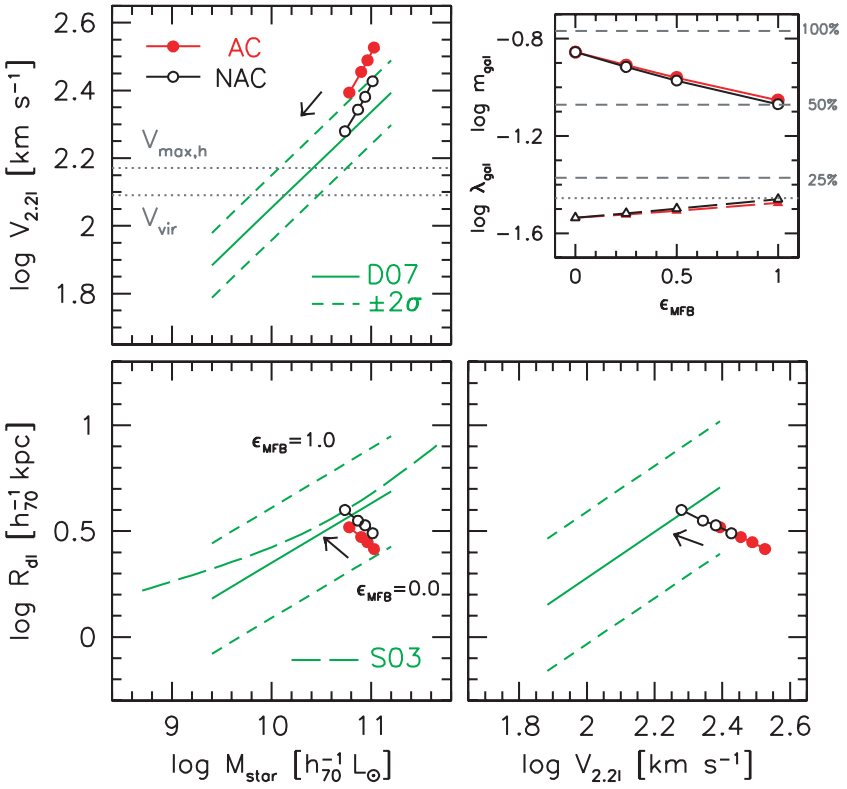

Figure 3. As Fig. 2, but for momentum-driven winds.

result in less efficient SF, and hence higher gas fractions and lower stellar masses. The reduction in the amount and density of the baryons results in a lower rotation velocity, both because the baryons contribute less to the circular velocity at 2.2 disc scalelengths and because there is less halo contraction. With a high-energy feedback efficiency of $\epsilon_{\rm EFB} = 1.0$, the galaxy formation efficiency drops to $\simeq$15 per cent: $\simeq$20 per cent of the baryons have not cooled, while $\simeq$65 per cent of the baryons have been ejected from the disc and halo. This model also has a galaxy spin a factor of $\simeq$1.7 higher than the halo spin. The low galaxy mass fraction and higher galaxy spin parameter result in sizes that are more than a factor of $\simeq$2 too large. The feedback efficiency can be tuned so that the model reproduces the size–mass or size–velocity relation. However, for all feedback efficiencies, the models rotate too fast at a given stellar mass. This is because higher feedback efficiency results in lower stellar masses as well as lower rotation velocities, with the net result that galaxies move almost parallel to the TF relation.

Fig. 3 shows the same results as Fig. 2, but for the momentum-driven wind model. Even with 100 per cent efficiency, this galaxy formation efficiency is $\simeq$50 per cent, where $\simeq$30 per cent of the baryons have been ejected from the disc and halo. This results in sizes that are in agreement with observations, but the models still rotate too fast. The reason that energy-driven winds are more efficient at ejecting mass than momentum-driven winds is shown in Fig. 4, which shows the mass loading factor, η, versus the wind velocity, $V_{\rm w}$. The mass loading factor is defined as the ratio between the mass outflow rate and the SFR. For energy-driven winds $\eta \propto V_{\rm w}^{-2}$, whereas for momentum-driven winds $\eta \propto V_{\rm w}^{-1}$. Thus everything being equal, energy-driven winds have higher mass loading factors than momentum-driven winds for all typical wind velocities

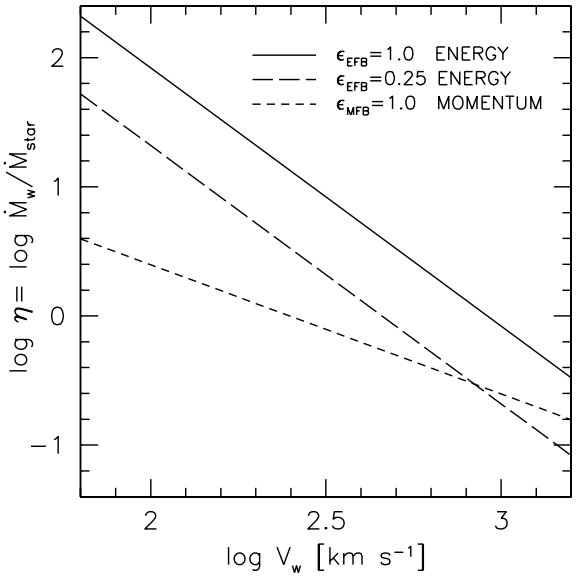

Figure 4. Mass loading factor versus wind velocity for energy- and momentum-driven winds. For equal efficiencies, energy-driven wind is always more efficient than momentum-driven wind, especially for low wind velocities.

3.3 The Tully–Fisher zero-point problem

A common problem to both feedback models, for all values of the feedback efficiency, is that they overpredict the rotation velocities. This is a standard problem for galaxy formation models in ΛCDM. As discussed in D07 and Gnedin et al. (2007), there are

three solutions: (1) lower the stellar-mass-to-light ratio (i.e. for a given luminosity there is less stellar mass which shifts observed galaxies to the left and hence higher velocity in the *VM* plane).[2] (2) Lower the initial halo concentration (which directly lowers $V_{2.2}$). (3) Reverse halo contraction (which directly lowers $V_{2.2}$).

A small change in the stellar-mass-to-light ratio would be plausible due to systematic uncertainties (such as in the IMF or the stellar populations synthesis models) in the measurement of stellar-mass-to-light ratios. However, the stellar-mass-to-light ratios would have to be lowered by about a factor of 2 to match the TF zero-point. Such a large change would require a top-heavy IMF. But all of the available constraints on stellar-mass-to-light ratios point to IMFs similar to Chabrier (e.g. de Jong & Bell 2007).

Lower halo concentrations would require less power on galaxy scales than in standard ΛCDM. This would also reduce the amount of substructure, which could help solve the missing satellite problem (Klypin et al. 1999; Moore et al. 1999). However, the recent discovery of many satellite galaxies around the Milky Way has lessened the discrepancy between observations and standard ΛCDM (e.g. Tollerud et al. 2008 and references therein). Furthermore, using cosmological simulations with parameters from the latest *WMAP* results (Spergel et al. 2007; Dunkley et al. 2009), Macciò et al. (2008) have shown that the central densities of dark matter haloes are consistent (both in normalization and scatter) with those measured from dwarf and LSB galaxies (which typically have maximum rotation velocities of $\simeq$100 km s^{-1}). Thus, there does not seem compelling evidence for a modification to ΛCDM on small scales.

Given that reducing stellar-mass-to-light ratios or the initial halo concentrations do not seem plausible, we consider the third possibility that haloes do not contract as expected. There are two processes that could cause the halo to expand. (1) Dynamical friction between baryons and the halo, e.g. by infalling baryonic clumps (e.g. El-Zant, Shlosman & Hoffman 2001; El-Zant et al. 2004; Tonini, Lapi & Salucci 2006; Jardel & Sellwood 2009) or by galactic bars (Weinberg & Katz 2002; Holley-Bockelmann et al. 2005; Sellwood 2008). (2) Rapid (i.e. non-adiabatic) mass loss from the galaxy, e.g. by SN-driven winds (Gnedin & Zhao 2002; Read & Gilmore 2005). Both of these effects have been shown to be effective at expanding the halo, but the combined effect (which may be greater than the sum of its parts) has so far not been investigated. Note that our standard model with adiabatic contraction takes into account the adiabatic expansion of the halo due to outflows. However, since there is a net inflow of baryons into the centres of galaxies, the overall effect is halo contraction.

Furthermore, halo contraction is based on the idea that galaxies form by cooling flows. The hot gas radiates away its binding energy, so when it falls to the centre of the potential to form the galaxy the halo has to contract. However, recent simulations have indicated that the gas, in haloes that host disc galaxies, is accreted by cold flows (i.e. it does not shock heat when it enters the virial radius). This new scenario thus allows the possibility of the baryons transferring energy to the halo during galaxy formation.

The black circles in Figs 2 and 3 show the results for two models without halo contraction. For both energy- and momentum-driven winds, the galaxy mass fractions and spin parameters have the same dependence on the feedback efficiency in models with and without halo contraction. However, the models without halo contraction have significantly lower rotation velocities, allowing a match to the TF zero-point for energy feedback efficiencies of $\simeq 0.1 - 0.5$, or momentum feedback efficiencies of $\simeq$1. A model with $\epsilon_{\rm EFB} = 0.25$ also has $V_{2.2I} \simeq V_{\rm max,h}$, and a galaxy formation efficiency of $\simeq$35 per cent, consistent with observations (see Section 1). However, this model has sizes that are too large. The solution to this is to lower the spin parameter of the baryons. This could occur if disc galaxies formed in haloes with lower than average halo spin, or by the baryons transferring some of their angular momentum to the halo during galaxy assembly, e.g. via dynamical friction. As we discussed above, such a process may be responsible for expanding the halo. As we show below, a model with a factor of 1.4 lower halo spin reproduces both *VM* and *RM* relations as well as low galaxy formation efficiencies. The momentum feedback model with maximum feedback efficiency $\epsilon_{\rm MFB} = 1.0$, on the other hand, roughly reproduces the *VM* and *RM* zero-points, but it has galaxy mass fractions and $V_{2.2I}/V_{\rm max,h}$ that are too high compared to observational and theoretical constraints.

3.4 Models with scatter

Having discussed the effects of energy- versus momentum-driven winds, and halo contraction versus no-halo contraction for a single halo mass, with the median concentration, and angular momentum parameters, we now turn our attention to models with the full range of halo masses relevant for disc galaxies, and with distributions of concentration, and angular momentum parameters.

We run a Monte Carlo simulations with halo masses ranging from $10^{10} \lesssim M_{\rm vir} \lesssim 10^{13}\, h^{-1}\, {\rm M}_\odot$, corresponding to virial velocities ranging from $31 \lesssim V_{\rm vir} \lesssim 310\,{\rm km\,s^{-1}}$. In ΛCDM, there are many more low-mass haloes than high-mass haloes, however, since we are interested in the scaling relations between galaxies, rather than the number densities we sample the halo masses uniformly in log-space.

As discussed in D07, we also find that models with the expected scatter in halo spin parameter $\sigma_{\ln\lambda} = 0.54$ significantly overpredict the amount of scatter in the *RM* and *RV* relations. This may signify that disc galaxies form in a special subset of haloes or that the baryons acquire a different distribution of specific angular momentum than the dark matter. For the remainder of this paper, we adopt $\sigma_{\ln\lambda} = 0.35$, as this provides a reasonable agreement to the observed scatter in disc sizes.

To illustrate the effect of feedback on galaxy scaling relations, we consider three models. Model I has no feedback, Model II has momentum feedback and Model III has energy feedback, and an average spin parameter a factor of 1.4 lower than Models I and II. The parameters of these models are given in Table 1. The parameters of Models II and III were chosen to match the zero-points of the *VMR* relations, and thus for reasons discussed above, they have no adiabatic contraction. For each model, we run a Monte Carlo simulation consisting of 2000 galaxies. For each galaxy, we select the parameters c, λ and α from lognormal distributions with means and scatters as determined by the parameters in Section 2.10 and Table 1.

Table 1. Model parameters.

Name	$\epsilon_{\rm EFB}$	$\epsilon_{\rm MFB}$	$\bar{\lambda}$	$\sigma_{\ln\lambda}$	AC
I: No feedback	0.0	0.0	0.035	0.35	N
II: Momentum	0.0	1.0	0.035	0.35	N
III: Energy	0.25	0.0	0.025	0.35	N

[2] Note that the stellar masses of the model galaxies are not completely independent of the IMF, as the return fraction is IMF-dependent. However, changes in the return fraction are compensated for by changes in the SFR.

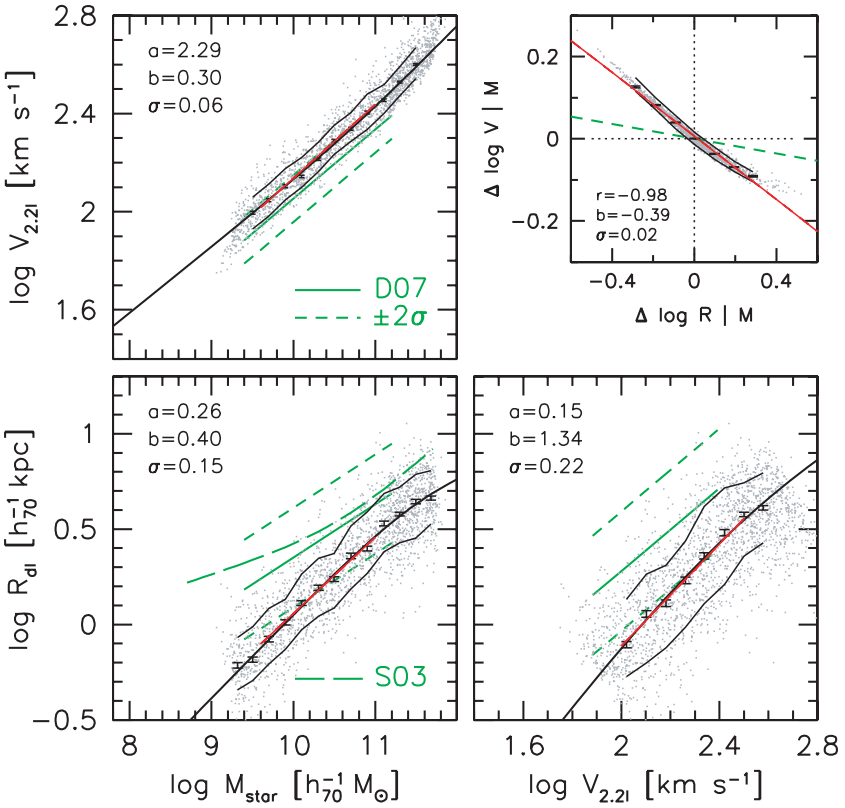

Figure 5. $V_{2.2I} - M_{\rm star} - R_{\rm dI}$ relations for Model I (no feedback) for virial masses logarithmically sampled in the range $10^{10} < M_{\rm vir} < 10^{13}\,h^{-1}\,{\rm M}_\odot$. The grey points and black lines show the models, while the green lines show the observed relations. In the *VMR* panels, the solid and dashed green lines show the mean and 2σ scatter, assuming a Chabrier IMF, of the observed relations from D07. In the *RM* panel, the long dashed green line shows the observed half-light radius–stellar-mass relation from Shen et al. (2003). In the $VM - RM$ residual panel, the green dashed line shows the observed correlation from Avila-Reese et al. (2008). The black lines show the 16th and 84th per centiles of the models, while the error bars show the Poisson error on the median. The thick black line shows a double power-law fit to the median using the function in equation (42), the parameters of the fits are given in Table 2. The solid red lines show the mean of the models fitted over a range corresponding to $10^{9.6} < M_{\rm star} < 10^{11.0}\,h_{70}^{-1}\,{\rm M}_\odot$. The parameters of the fits [zero-point, slope, scatter (in $\log_{10}$ units)] are given in the top-left corner of each panel. The relations are fitted as follows: $\log V = a + b(\log M - 10.5)$; $\log R = a + b(\log M - 10.5)$; $\log R = a + b(\log V - 2.195)$. The upper-right panel shows the residuals of the *VM* relation versus the residuals of the *RM* relation. The red lines show the mean and 1σ scatter of a fit of the form: $\Delta\log V\,|M = b\,\Delta\log R\,|M$. The correlation coefficient, r, is also given where $r = b\,\sigma_x/\sigma_y$, where $x = \Delta\log R \mid M$ and $y = \Delta\log V \mid M$. This model fails to reproduce all of the observations (with the exception of the slope of the *VM* relation).

Figs 5–7 show the *VMR* relations, as well as the correlation between the residuals of the *VM* and *RM* relations, for Models I–III. Recall that V is the circular velocity measured at 2.15 I-band disc scalelengths, M is the stellar mass and R is the I-band disc scalelength.

3.4.1 Slopes

The VMR relations in these figures are fit with two relations: a single power law over the range where there is observational data, and a double power law over the full range of masses. The parameters of the best-fitting single power-law fits are indicated in the panels of Figs 5–7. The double power law is given by

$$y = y_0 \left(\frac{x}{x_0}\right)^{\alpha} \left[\frac{1}{2} + \frac{1}{2}\left(\frac{x}{x_0}\right)\right]^{(\beta-\alpha)} . \qquad (42)$$

Here, α is the slope at $x \ll x_0$, β is the slope at $x \gg x_0$, x_0 is the transition scale and y_0 is the value of y at x_0. The best-fitting values of these parameters are given in Table 2.

The slope (as given by the single power-law fits) of the *VM* relation is only weakly dependent on the feedback model. This is expected since (as shown in Figs 2 and 3) the offset of a galaxy from the *VM* relation is only weakly dependent on the galaxy mass fraction, which is determined by feedback (for haloes with $M_{\rm vir} \lesssim 10^{12}\,{\rm M}_\odot$). By contrast, the slope of the *RM* relation depends strongly on the feedback model. Again, this is expected given that the offset of a galaxy from the *RM* relation depends strongly on the galaxy mass fraction. The model without feedback (Model I) has a slope of 0.40, the model with momentum-driven feedback (Model II) has a slope of 0.26 and the model with energy-driven feedback (Model III) has a slope of 0.14.

The observed slope of the size–mass relation from Courteau et al. 2007 and D07 is $\simeq$0.28, which favours the momentum-driven wind model. However, as discussed in Section 3.1, at low stellar masses ($M_{\rm star} \lesssim 10^{10}\,{\rm M}_\odot$), this slope is likely biased high by selection effects. Shen et al. (2003) find a slope of 0.14 at low masses for the half-light radius–stellar-mass relation for a much more complete sample of late-type galaxies. Such a shallow slope is in much better agreement with our energy-driven model. Thus the observed slope of the *RM* relation favours the energy-driven wind model at low masses, and the momentum-driven model at high masses. However, at high stellar masses ($M_{\rm star} \gtrsim 10^{10.5}\,{\rm M}_\odot$) bulges are common is spiral galaxies (e.g. Weinzirl et al. 2009). Due to the correlation between the masses of bulges and black holes (Magorrian et al.

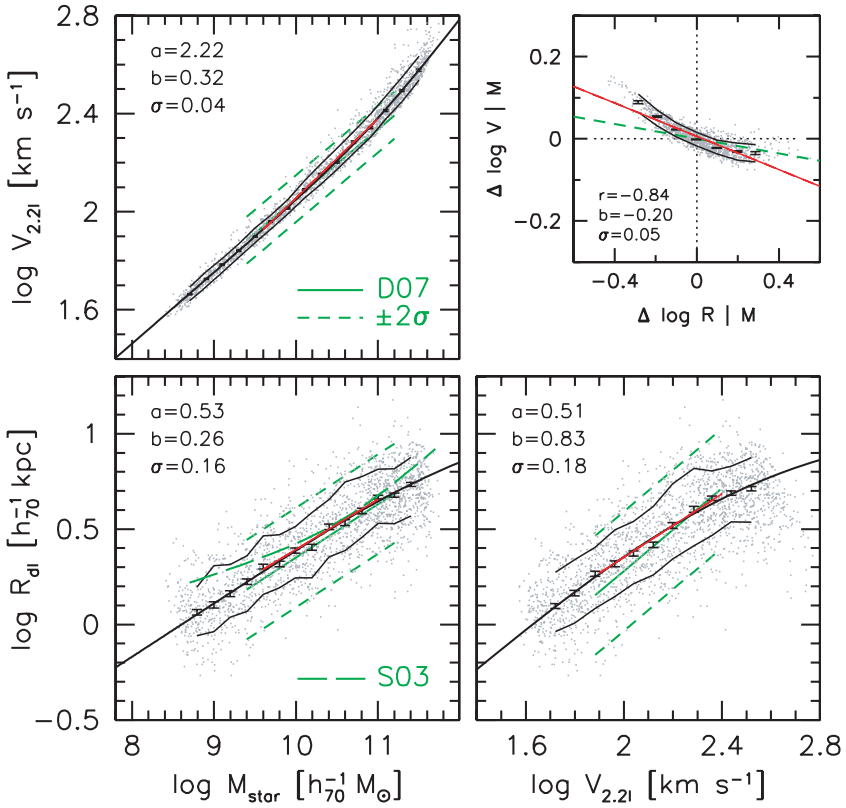

Figure 6. As Fig. 5, but for Model II (momentum-driven feedback). This model provides a reasonable match to the zero-points, slopes and scatters of the *VMR* relations.

1998), active galactic nuclei (AGN) feedback may play a significant role in regulating galaxy formation efficiency in high-mass spiral galaxies. Thus it is *plausible* that a model with energy-driven SN feedback (which primarily effects galaxies in low-mass haloes) and AGN feedback (which primarily effects galaxies in high-mass haloes) could explain the slopes of the size–mass relation at low and high masses. However, since AGN feedback is not expected to be significant for galaxies in low-mass haloes, it is *unlikely* that AGN feedback will be able to help the momentum-driven wind model to reproduce the shallow slope of the size–mass relation at low masses.

3.4.2 Scatter and residual correlations

All models produce a *VM* relation with relatively small scatter, with smaller scatter in the models with feedback. The amount of scatter in the *VM* relation is directly related to the strength of the correlation between the *VM* and *RM* relations. The model without feedback has a very strong correlation (correlation coefficient, $r = -0.98$; slope, $b = -0.39$), which is caused by these galaxies being baryon dominated at 2.2 disc scalelengths. The models with feedback have weaker, but still significant, correlations ($r \simeq -0.8$, $b \simeq -0.2$). These correlations are stronger than that observed by Courteau et al. (2007) for the *I*-band *VL* and *RL* relations ($r = -0.16$, $b = -0.07$), and by Gnedin et al. (2007) ($r = 0.23 \pm 0.14$) and Avila-Reese et al. (2008) ($r = -0.29$, $b = -0.09$) for the stellar mass *VM* and *RM* relations. However, as discussed in D07, scatter in the stellar-mass-to-light ratio of $\simeq$0.15 dex either from intrinsic variations or from measurement uncertainties will weaken the correlation between the observed relations compared to the theoretical *VM* and *RM* relations. Thus we do not consider this failure of the model as a serious shortcoming.

3.5 The baryonic Tully–Fisher relation

The fundamental basis of the TF (linewidth–luminosity) relation is believed to be the relation between the asymptotic rotation velocity of a galaxy disc, $V_{\rm flat}$, and the baryonic mass, $M_{\rm gal}$ (the sum of stellar and cold gas mass). This relation is referred to as the Baryonic Tully–Fisher (BTF) relation. It was first studied by McGaugh et al. (2000), and subsequently by Bell & de Jong (2001), McGaugh (2005), Geha et al. (2006), Noordermeer & Verheijen (2007) and Avila-Reese et al. (2008).

The most significant source of uncertainty in the BTF is how one measures stellar mass. McGaugh (2005) measured the BTF for stellar masses calculated using different methods: stellar population synthesis models (e.g. Bell & de Jong 2001), the maximum disc hypothesis (van Albada & Sancisi 1986) and the mass-discrepancy acceleration relation [i.e. Modified Newtonian Dynamics (MOND); Milgrom 1983]. McGaugh (2005) found that the scatter in the BTF was minimized when the stellar masses were calculated with the mass-discrepancy acceleration relation. Under the assumption that the correct method would minimized the scatter in the BTF, this is evidence in favour of MOND over dark matter.

However, this is a circular argument because a relation between the asymptotic rotation velocity of a galactic disc, $V_{\rm flat}$, and the baryonic mass, $M_{\rm gal}$, with *zero scatter* is built into MOND. Thus if the stellar masses are chosen based on the MOND prescription, they will result in a BTF with scatter only due to measurement errors on $V_{\rm flat}$ and distance uncertainties. The scatter in the BTF

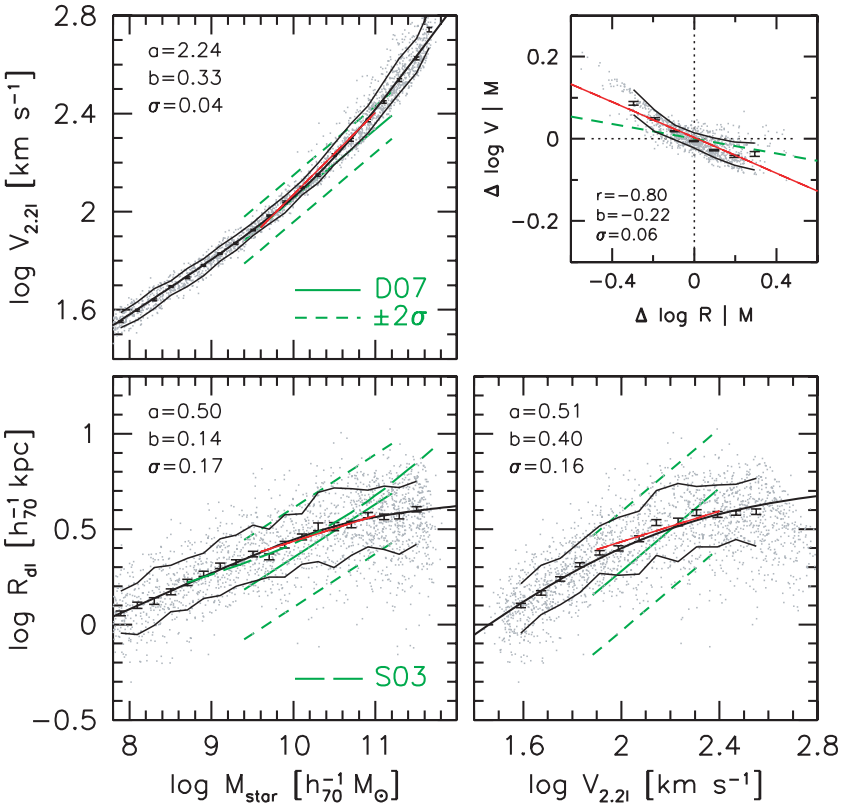

Figure 7. As Fig. 5, but for Model III (energy-driven feedback). This model provides a reasonable match to the zero-point, slope and scatter of the *VM* relation. It predicts a shallower slope to the *RM* and *RV* relations than our fiducial data from D07, however at low masses the shallow slope of the model is in good agreement with the data from Shen et al. (2003) (green long dashed). The correlation between the residuals of the *VM* and *RM* relations (top-right panel) of the models is stronger than the observations, although observational uncertainties in stellar mass measurements will cause the observed correlation to be underestimated.

Table 2. Parameters of double power-law fits to *VMR* relations in Figs 5–7 using the function in equation (42) .

Model	α	β	$M_{\rm star,0}$	$V_{2.2I,0}$
I	0.27	0.34	10.71	2.34
II	0.29	0.44	10.94	2.36
III	0.22	0.46	10.35	2.17
Model	α	β	$M_{\rm star,0}$	$R_{\rm dI,0}$
I	0.44	0.14	11.56	0.65
II	0.28	0.17	11.15	0.68
III	0.19	0.04	10.55	0.52
Model	α	β	$V_{2.2I,0}$	$R_{\rm dI,0}$
I	1.79	0.40	2.59	0.65
II	1.15	0.00	2.50	0.72
III	1.15	0.00	2.00	0.40

(as defined as the relation between $V_{\rm flat}$ and $M_{\rm gal}$) thus cannot be used to discriminate between MOND and dark matter. However, MOND generally predicts higher stellar masses than stellar population synthesis models (based on a Kroupa IMF). Thus if stellar masses could be measured independently, this would provide a means of falsifying MOND.

Here, we use the data from McGaugh (2005), using the stellar population synthesis stellar-mass-to-light ratios, with an offset of -0.1 dex (corresponding to a Chabrier IMF). The majority of galaxies in this sample are in the UMa cluster, for which the distance is somewhat uncertain. McGaugh (2005) adopted a distance of 15 Mpc. We adopt the *Hubble Space Telescope* Key Project distance of $D = 20.7$ Mpc (Sakai et al. 2000), which is also the distance used by Bell & de Jong (2001).

The BTF data are plotted as green filled circles in Fig. 8. A linear fit to the data gives the following relation between the rotation velocity and baryonic mass:

$$\log \frac{V_{\rm flat}}{({\rm km\,s^{-1}})} = 2.027 + 0.279 \left[\log \frac{M_{\rm gal}}{({\rm M_\odot})} - 10 \right] \qquad (43)$$

with a scatter of 0.053 dex in $\log V_{\rm flat}$. This BTF is consistent with that from Bell & de Jong (2001) who report a slope of 0.285 ($\pm$0.015) and a zero-point of 2.031($\pm$0.011), and that from Avila-Reese et al. (2008) who report a slope of 0.306($\pm$0.012) a zero-point of 2.036($\pm$0.129) and an intrinsic scatter of 0.051 dex in $\log V$. The slightly steeper slope obtained by Avila-Reese et al. (2008) can be attributed (see Verheijen 2001) to their use of H I linewidths, compared to $V_{\rm flat}$ used by McGaugh (2005) and Bell & de Jong (2001). This good agreement is reassuring given that the data samples are largely based on the data set of Verheijen et al. (2001).

The BTF relations for our models are given by the grey dots in Fig. 8. For the rotation velocity, we use $V_{\rm 80c}$, the circular velocity at a radius enclosing 80 per cent of the gas mass, $R_{\rm 80c}$, which usually corresponds to the flat part of the rotation curve (see e.g. Dutton 2009 rotation curves). Power-law fits to the models over baryonic masses between 1×10^9 and 1×10^{11} are shown as red lines in the figure. The parameters of these fits are given in the top-left corner of each panel. All three models result in BTF relations with similar slopes, zero-points and scatter, and in reasonable agreement with

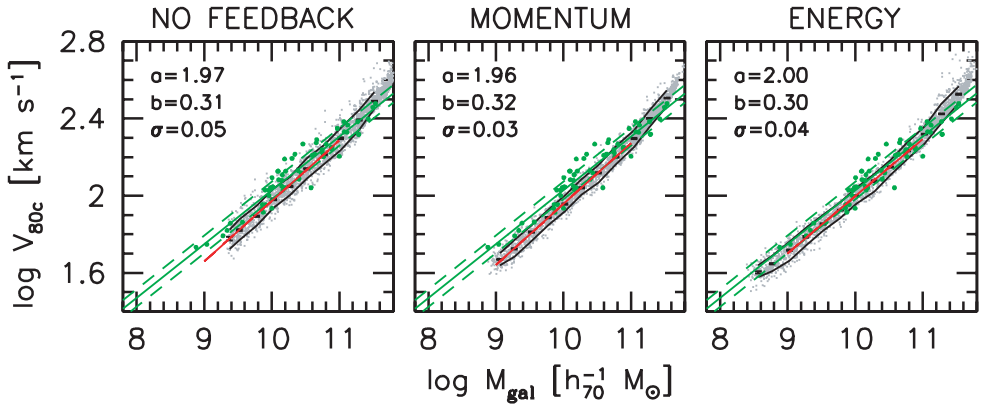

Figure 8. Dependence of the BTF relation at redshift $z = 0$ on feedback. The green points show data from McGaugh (2005), where the rotation velocities have been measured in the 'flat' part of resolved HI rotation curves. Green lines show the mean and 1σ scatter of a fit to this data. The grey points show the models, where V_{80c} is the circular velocity at a radius enclosing 80 per cent of the gas. The black lines show the 16th and 84th percentiles in bins of width 0.25 dex in M_{gal}. The red lines show a fit of the form: $\log V_{80c} = a + b(\log M_{gal} - 10)$. The fits are performed over the range that the red lines are plotted. The zero-point, slope and scatter for each fit are given in the upper-right corner of each panel. The slope, zero-point and scatter of the BTF relation are only weakly dependent on the feedback model.

observations. We note that for the model galaxies the slope of the BTF depends on galaxy mass, with slightly larger slopes for higher mass galaxies.

The BTF relation has been used to constrain the relation between baryonic mass and halo mass. By comparing the observed slope of the BTF (0.27 ± 0.01) to the prediction from CDM (the slope of the $V_{max,h} - M_{vir}$ relation for dark matter haloes is 0.294 ± 0.005, Bullock et al. 2001a), Geha et al. (2006) argued that low-mass galaxies have not preferentially lost baryons as would be predicted by feedback models (e.g. Dekel & Silk 1986). However, this is based on the incorrect assumption that the maximum observed rotation velocity is equal (or proportional) to the maximum circular velocity of the halo, *independent* of the baryon to halo mass ratio. As discussed by several authors (e.g. Navarro & Steinmetz 2000; D07; Avila-Reese et al. 2008), the maximum rotation velocity of a galaxy is, in general, not equal to the maximum circular velocity of the halo in the absence of galaxy formation, $V_{max,h}$. As the baryon fraction increases, so does the maximum circular velocity. This is because the baryons contribute a non-negligible amount of mass to the circular velocity. Thus for reasonable galaxy mass fractions, variation in galaxy mass fraction moves galaxies roughly parallel to the BTF.

Fig. 8 shows that the slope, zero-point and scatter of the BTF are remarkably insensitive to the feedback model. Furthermore, as shown in Section 4.1, our energy feedback model results in substantial differential mass loss between haloes of mass $M_{vir} \simeq 10^{10}$ and $10^{12}\,M_\odot$. Yet it has the same BTF slope as a model with no mass loss (and constant baryon to dark matter ratio within this range of halo masses). This provides a counter example to the claim by Geha et al. (2006) that models with preferential mass loss in dwarf galaxies cannot explain the slope of the BTF.

4 THE DEPENDENCE OF GALAXY MASS FRACTIONS AND SPIN PARAMETERS ON FEEDBACK

The two main parameters that determine the structure of disc galaxies are the mass and specific angular momentum of the cold gas and stars. We now investigate the dependence of these parameters on feedback and halo mass.

4.1 Galaxy mass fractions

Fig. 9 shows the mass fractions and spin parameters of our three models as a function of virial mass.

The relations in Fig. 9 are fitted with the following double power law:

$$y = y_0 \left(\frac{x}{x_0}\right)^{\alpha} \left[\frac{1}{2} + \frac{1}{2}\left(\frac{x}{x_0}\right)^{\gamma}\right]^{(\beta-\alpha)/\gamma}. \quad (44)$$

Here, α is the slope at $x \ll x_0$, β is the slope at $x \gg x_0$, x_0 is the transition scale, y_0 is the value of y at x_0 and γ determines how fast the transition is. The best-fitting values of these parameters are given in Table 3.

We start our discussion with Model I, which has no feedback (left-hand panels). For low-mass haloes, the galaxy mass fraction m_{gal} is close to the universal baryon fraction, $f_{bar} \simeq 0.17$. This is because cooling is very efficient in low-mass haloes. Above a halo mass of $M_{vir} \simeq 10^{12}\,M_\odot$, the galaxy mass fraction drops significantly, due to the inefficiency of cooling in high-mass haloes. We hereafter refer to this mass scale as the cooling threshold.

The effect of feedback is to remove cold gas from the galaxy–halo system. The efficiency with which feedback can eject gas depends on the depth of the potential well, the amount of SF and on the wind model. The net effect in both energy and momentum wind models is for mass to be lost preferentially in lower mass haloes (i.e. potential well dominates over SF efficiency at fixed halo concentration and angular momentum parameters). Note the fraction of mass lost varies smoothly with virial mass, i.e. there is no threshold for mass loss, as for example there would be in a constant wind velocity model. However, the energy-driven wind model is much more efficient at removing baryons from haloes below $M_{vir} \simeq 10^{12}\,M_\odot$. This results in very different scalings between m_{gal} and m_{star} with M_{vir} for the two feedback models. The parameters of these scalings are given in Table 3. In principle, these differences are testable with galaxy–galaxy weak lensing and/or satellite kinematics measurements of virial masses, combined with measurements of stellar masses and neutral hydrogen gas masses. For both feedback models, the maximum galaxy formation efficiency (defined as m_{gal}/f_{bar}) occurs around a virial mass of $M_{vir} \simeq 10^{12}\,M_\odot$, and is $\simeq$0.50 for the momentum-driven wind and $\simeq$0.35 for the energy-driven winds.

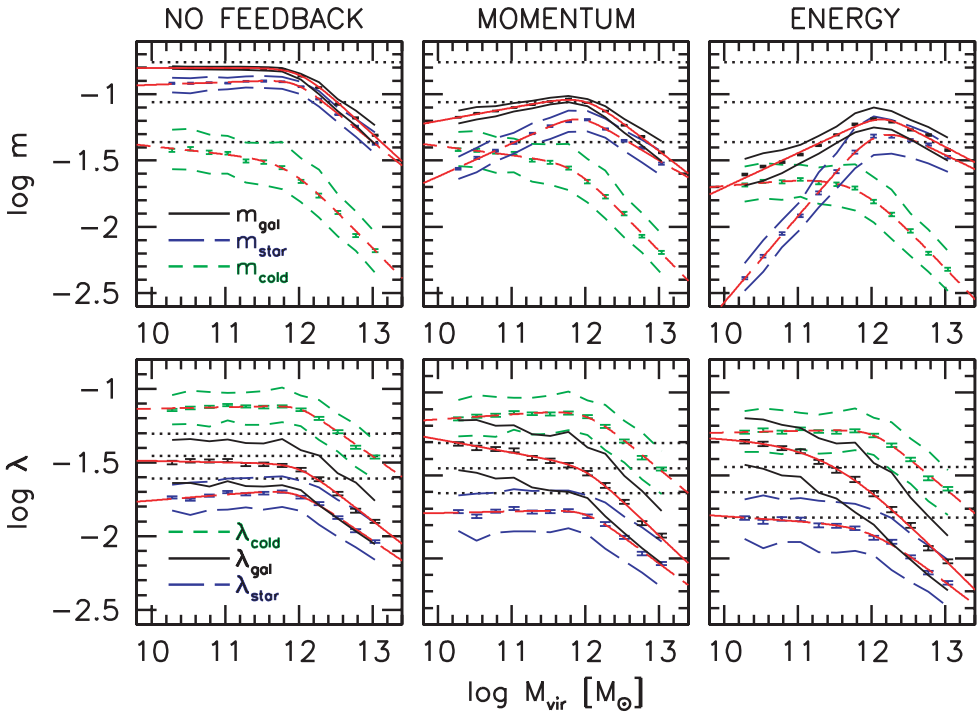

Figure 9. Dependence of mass fractions and spin parameters on virial mass for our three feedback models: no feedback (left-hand panels); momentum feedback (middle panels) and energy feedback (right-hand panels). The lines show the 16th and 84th percentiles in bins of width 0.25 dex in $M_{\rm vir}$, the error bars show the Poisson error on the median. The upper panels show the mass fractions of the galaxy, $m_{\rm gal} = M_{\rm gal}/M_{\rm vir}$ (black, solid); stars, $m_{\rm star} = M_{\rm star}/M_{\rm vir}$ (blue, long dashed) and cold gas $m_{\rm cold} = M_{\rm cold}/M_{\rm vir}$ (green, short dashed). The dotted lines show the cosmic baryon fraction, $f_{\rm bar}$, as well as $f_{\rm bar}/2$, and $f_{\rm bar}/4$. The red lines show double power-law fits to the medians, the parameters of these fits are given in Table 3. The lower panels show the spin parameters of the galaxy, $\lambda_{\rm gal} = (j_{\rm gal}/m_{\rm gal})\lambda$ (black, solid); stars, $\lambda_{\rm star} = (j_{\rm star}/m_{\rm star})\lambda$, (blue, long dashed); cold gas, $\lambda_{\rm cold} = (j_{\rm cold}/m_{\rm cold})\lambda$ (green, short dashed) and dark matter, λ, (black, dotted).

Fig. 9 also shows the cold gas mass fraction $m_{\rm cold}$, which is just the difference between $m_{\rm gal}$ and $m_{\rm star}$. Below the cooling threshold, $m_{\rm cold}$ is almost independent of $M_{\rm vir}$, while above the cooling threshold $m_{\rm cold}$ strongly decreases with $M_{\rm vir}$. These trends of $m_{\rm cold}$ with $M_{\rm vir}$ are qualitatively similar for all three feedback models. Thus feedback has a much stronger impact on the stellar mass fraction, $m_{\rm star}$, than on the cold gas mass fraction, $m_{\rm cold}$.

4.2 Galaxy spin parameters

The assumption that $(j_{\rm gal}/m_{\rm gal}) = 1$ underlies most applications of the MMW disc structure models, as well as observational attempts at measuring the halo spin parameter (e.g. van den Bosch, Burkert & Swaters (2001). Thus an important question is whether this assumption is valid in galaxy formation models that include inflows and outflows.

The lower panels of Fig. 9 show the spin parameters of our three models as a function of virial mass. We first discuss the model without feedback. For haloes below the cooling threshold, the spin parameter of the galaxy, $\lambda_{\rm gal}$, is almost the same as that of the dark matter, which is because almost all of the baryons have cooled, and thus they bring in almost all of the angular momentum. However, for haloes above the cooling threshold, $\lambda_{\rm gal}$ decreases by about a factor of 2 from $M_{\rm vir} = 10^{12}$ to $10^{13}\,{\rm M}_{\odot}$. This is because the highest angular momentum material virializes at low redshifts, and this gas does not have time to cool.

As would be expected, the stellar mass fraction and spin parameters are lower than the corresponding parameters for the total galaxy. The lower stellar spin parameters are due to the SF law, which causes stars to form less efficiently at larger radii (where the gas density is lowest). Thus the gas disc is more extended that the stellar disc.

An interesting result of our models with feedback is that the galaxy spin parameter can be higher than the halo spin parameter. This is because mass can only be ejected from radii where there is SF, and these are biased towards small radii, where the specific angular momentum of the gas is lower than the average. As shown below (in Section 4.3), at a given halo mass, feedback is more efficient at removing baryons from higher surface density discs. Thus the increased SF efficiency overcomes the deeper potential well. Note that the scatter in the galaxy and stellar spin parameters is roughly equal to the scatter in the halo spin parameter, and this does not change with virial mass.

Although the spin parameters of the galaxy and stars are typically different from that of the halo, Fig. 10 shows that the ratio of the specific angular momentum of the baryons to that of the dark matter $(j_{\rm gal}/m_{\rm gal})$ at a given virial mass has very little scatter (0.01 dex for Model I, 0.02 dex for Model II and 0.04 dex of Model III). The small scatter holds for all halo masses, even for galaxies that have lost more than half of their baryons. The small scatter is related to the fact that there is very little scatter in the baryon mass fraction at a given halo mass. By contrast there is a much larger scatter (0.07–0.08 dex) in the ratio between the specific angular momentum of the stars and the dark matter. This is due to the dependence of global SF efficiency on galaxy surface density.

Given that the assumption that $(j_{\rm gal}/m_{\rm gal}) = 1$ is violated in all of our models, care should be taken when interpreting models and observational results based on this assumption. However, in

Table 3. Parameters of double power-law fits to mass fractions and spin parameters versus virial mass in Fig. 9 using the function in equation (44) .

Model	α	β	γ	$M_{\rm vir,0}$	$m_{\rm cold,0}$
I	−0.06	−0.57	2.00	11.85	−1.58
II	−0.07	−0.57	2.45	11.84	−1.58
III	0.05	−0.59	1.50	11.80	−1.73
Model	α	β	γ	$M_{\rm vir,0}$	$m_{\rm star,0}$
I	0.02	−0.45	3.54	11.96	−0.93
II	0.25	−0.33	3.60	11.92	−1.19
III	0.65	−0.27	2.55	12.09	−1.32
Model	α	β	γ	$M_{\rm vir,0}$	$m_{\rm gal,0}$
I	0.00	−0.51	2.59	12.02	−0.86
II	0.10	−0.43	2.71	12.01	−1.06
III	0.26	−0.29	3.90	12.14	−1.19
Model	α	β	γ	$M_{\rm vir,0}$	$\lambda_{\rm cold,0}$
I	0.01	−0.35	4.14	12.02	−1.14
II	0.03	−0.37	2.45	12.03	−1.15
III	0.01	−0.37	2.95	12.03	−1.26
Model	α	β	γ	$M_{\rm vir,0}$	$\lambda_{\rm star,0}$
I	0.04	−0.34	2.79	11.97	−1.72
II	0.01	−0.33	3.10	12.02	−1.74
III	−0.03	−0.34	1.75	12.01	−1.86
Model	α	β	γ	$M_{\rm vir,0}$	$\lambda_{\rm gal,0}$
I	−0.01	−0.39	2.80	12.01	−1.55
II	−0.08	−0.42	2.70	12.00	−1.48
III	−0.02	−0.45	0.95	11.44	−1.44

our models there is very little scatter in $(j_{\rm gal}/m_{\rm gal})$ at a fixed halo mass. This suggests that the scatter in the galaxy spin parameter (which is in principle observable), at a given halo mass, may be an accurate reflection of the scatter in the halo spin parameter (which is a prediction of Λ CDM, but not directly observable).

4.3 Is galaxy mass fraction correlated with halo spin?

Fig. 9 shows that at a given virial mass there is only a small scatter in galaxy or stellar mass fractions. For the momentum-driven wind model, the scatter in $m_{\rm gal}$ and $m_{\rm star}$ is ≃8 and ≃20 per cent, respectively. For the energy-driven wind model, the scatters are ≃20 and ≃33 per cent, respectively.

We now turn to the question of where this scatter comes from. The upper panels of Fig. 11 show the residuals of the $m_{\rm gal} - M_{\rm vir}$ relations versus scatter in the halo spin parameter. For the no feedback model, the baryon fraction is determined by the efficiency of cooling. In our model, the cooling efficiency is to the first order determined by the halo mass. The very small scatter in $m_{\rm gal}$ results from scatter in the halo concentration, which effects the cooling in two ways. The halo concentration determines the MAH (i.e. low-concentration haloes collapse later, and thus there is less time for the baryons to cool). The halo concentration effects the density of the hot gas, which directly effects the cooling time. For the energy and momentum wind models, there is a positive correlation ($r \simeq 0.6$) between $m_{\rm gal}$ and λ at a given $M_{\rm vir}$. Thus at a given virial mass, galaxies that have lower spins (i.e. higher surface density discs) are more efficient at removing baryons, despite the deeper potential well.

The lower panels of Fig. 11 show the residuals of the $m_{\rm star} - M_{\rm vir}$ relations. All models show an anticorrelation between the residuals, i.e. galaxies that form in lower spin haloes are more efficient at turning their cold baryons into stars. This effect is expected from the density-dependent SF recipe that we adopt.

These results have implications for the scatter in the TF relation. As discussed in Section 1, one of the surprising aspects of the TF relation is that the scatter is independent of surface brightness, or equivalently the scatter in the *VL* relation is independent of the scatter in the *RL* relation. Firmani & Avila-Reese (2000), van den Bosch (2000) and D07 have shown that this could partially be explained by the dependence of gas fractions on surface density, such that lower surface density discs have higher gas fractions. Gnedin et al. (2007), on the other hand, invoked a correlation between disc mass fraction and disc surface density to reduce the correlation between the *VM* and *RM* relations. This works as follows. At a given stellar mass, there is a range in disc sizes. Smaller discs should result in larger $V_{2.2}$, both because the baryons contribute more to $V_{2.2}$ and because the halo contribution increases due to halo contraction. However, if the smaller discs live in lower mass haloes, then the reduced contribution of the halo compensates for the increased contribution from the disc. This should result in a negative correlation between $m_{\rm gal}$ and λ, opposite to what we find in our models. Gnedin et al. (2007) speculated that feedback would be less efficient in higher surface density discs, presumably because the potential well is deeper. However, in our models, the reverse is the case. At a given halo mass, higher surface density discs are more efficient at removing baryons because there is more energy (or momentum) input from SN due to the higher SFRs.

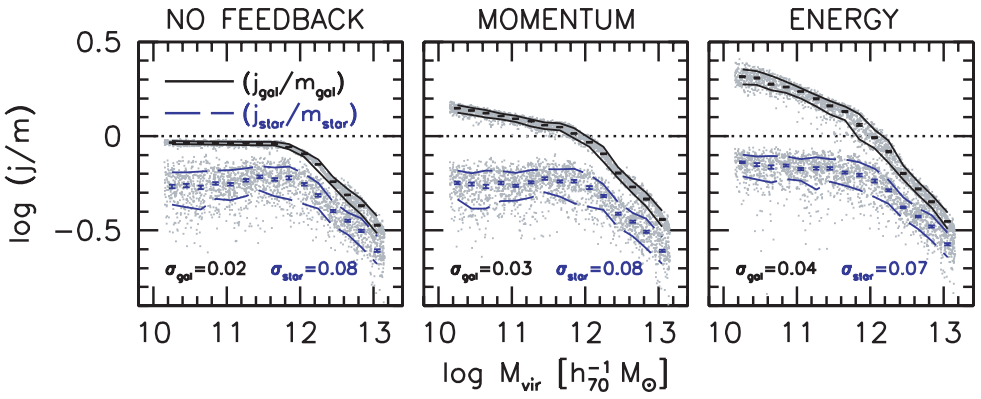

Figure 10. Dependence of ratio between the specific angular momentum of the baryons/stars (black/blue) and dark matter on virial mass for our three models. The lines show the 16th and 84th percentiles in bins of width 0.25 dex in $M_{\rm vir}$. The scatter about the median relation is given by $\sigma_{\rm gal}$ for $(j_{\rm gal}/m_{\rm gal})$ and $\sigma_{\rm star}$ for $(j_{\rm star}/m_{\rm star})$. The dotted line corresponds to the specific angular momentum of the baryons and stars being equal to that of the dark matter.

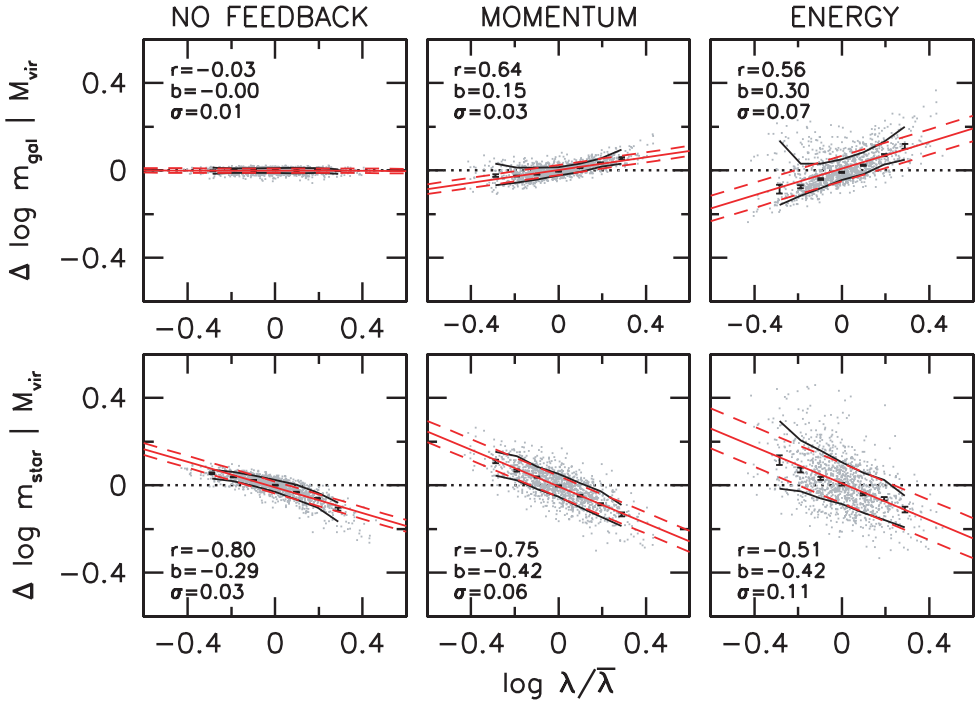

Figure 11. Correlation between scatter (at a given halo mass) in halo spin, with scatter (at a given halo mass) in galaxy mass fraction (upper panels) and stellar mass fraction (lower panels). The black lines show the medians 16th and 84th percentiles of the models. The scatter in the galaxy mass fraction is correlated with halo spin (i.e. feedback is more efficient in higher density galaxies), whereas the scatter in stellar mass fractions is anticorrelated with halo spin (i.e. SF is more efficient in higher density galaxies). The red lines show the mean (solid) and 1σ scatter (dashed) of a fit of the form: $\Delta \log m = b \log \lambda/\bar{\lambda}$. The slope, b, scatter, σ (in $\log_{10}$ units), and the correlation coefficient, r, are given for each fit. The correlation coefficient is given by $r = b\,\sigma_x/\sigma_y$, where $x = \log \lambda/\bar{\lambda}$ and $y = \Delta \log m \mid M_{\rm vir}$.

4.4 The dependence of gas fractions on feedback

Observationally it is known that the cold gas fraction is higher in lower mass galaxies (e.g. McGaugh & de Block 1997; Kannappan 2004; Avila-Reese et al. 2008). Here, we use data from Garnett (2002), who compiled B-band magnitudes, $B - V$ colours, atomic gas mass and molecular gas mass for 31 spiral galaxies and 13 irregular galaxies. We compute stellar masses using the following relation from Bell et al. (2003): $\log(M_{\rm star}/L_B) = -0.941 + 1.737\,(B - V) - 0.1$, where the -0.1 corresponds to a Chabrier IMF. The gas fractions, defined as $f_{\rm gas} = M_{\rm cold}/(M_{\rm cold} + M_{\rm star})$, versus stellar masses thus derived are plotted in green in Fig. 12. A linear fit gives the following relation between the gas fraction and logarithm of stellar mass:

$$f_{\rm gas} = 0.374 - 0.162\left[\log\frac{M_{\rm star}}{(h_{70}^{-2}\,{\rm M}_\odot)} - 10\right] \qquad (45)$$

with a scatter of 0.11 in $f_{\rm gas}$. Note that the ratio between atomic and molecular is a strong function of stellar mass. Massive galaxies have roughly equal amounts of atomic and molecular gas, while

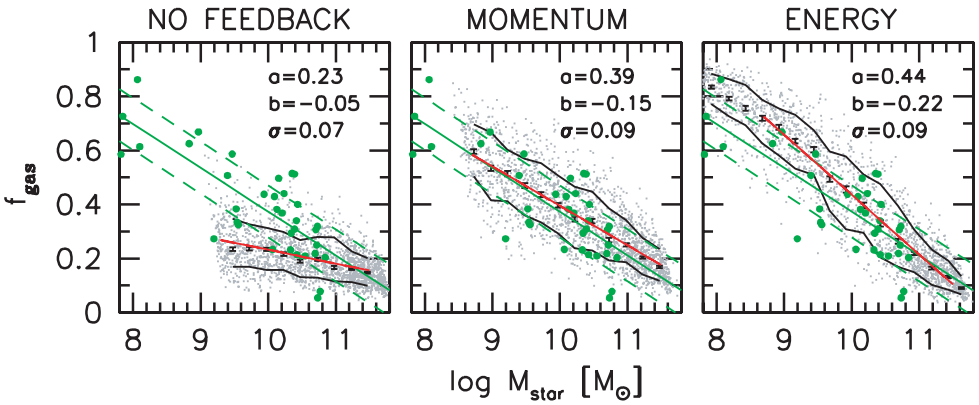

Figure 12. Dependence of the gas-fraction–stellar-mass relation at redshift $z = 0$ on feedback. The green points show data from Garnett (2002), with green lines showing the mean and 1σ scatter. The grey points show the models. The black lines show the 16th and 84th percentiles in bins of width 0.25 dex in $M_{\rm star}$. The red lines show a fit of the form: $f_{\rm gas} = a + b(\log M_{\rm star} - 10)$. The fits are performed over the range that the red lines are plotted. The zero-point, slope and scatter for each fit are given in the upper-right corner of each panel. Note that models and data include both atomic and molecular gas. The model without feedback underpredicts the gas fractions, whereas the models with feedback provide good matches to the observations.

the molecular gas fraction is negligible in galaxies with $M_{\rm star} \lesssim 10^{10}\,{\rm M}_{\odot}$. Thus ignoring the molecular gas significantly underestimates the gas fractions at the high-mass end.

Fig. 12 shows the gas fraction versus stellar mass relation for our three models at redshift $z = 0$. The models are given by the grey points. The model with no feedback (left-hand panel) results in gas fractions that are too low compared to the observations (green points and lines). This is a result of the discs being too high density, which causes SF to proceed too fast. Both models with feedback result in gas fractions that are in good agreement with observations (slope, zero-point and scatter). In particular, the momentum-driven wind model is almost indistinguishable from the observations. Distinguishing between these two feedback models would require a more complete sample of galaxies with robust atomic and molecular gas masses.

5 THE DEPENDENCE OF THE MASS–METALLICITY RELATION ON FEEDBACK

The relation between stellar mass (or luminosity) and gas (or stellar) phase metallicity has long been thought to hold important clues to the nature of galaxy outflows. Indeed, the slope of the mass–metallicity relation at $z \simeq 2$ has been used to argue in favour of momentum-driven outflows over energy-driven outflows and no outflows (Finlator & Davé 2008). However, the energy-driven wind model adopted in Finlator & Davé (2008) assumed a constant mass loading factor, $\eta = 2$, and a constant wind velocity $V_{\rm w} = 484\,{\rm km\,s^{-1}}$. As noted by Finlator & Davé (2008), this constant wind model is only one possible implementation of energy-driven outflows. Thus an interesting question is whether the energy-driven outflow model that we have implemented is able to reproduce the slope of the mass–metallicity relation at $z \simeq 2$.

Fig. 13 shows the stellar-mass–metallicity relation for our three models at redshift $z = 2.26$. The metallicity used here is the metallicity of the cold gas, which is calculated as the sum of metals in the cold gas divided by the mass of cold gas. The model with no feedback has a mass–metallicity relation with very shallow slope of $b \simeq 0.06$, and a mean metallicity close to that of the yield (i.e. solar). The green points with error bars show the observational results for the gas phase oxygen abundance versus stellar mass from Erb et al. (2006), assuming a solar oxygen abundance of $12 + \log({\rm O/H}) = 8.66$. Our no feedback model is inconsistent with the observations, in terms of both slope and zero-point. The models with feedback result in steeper slopes of the mass–metallicity relations: $b \simeq 0.17$ for the momentum wind model and $b \simeq 0.32$ for the energy wind model. Both of these models are in qualitative agreement with the observations. Overall the energy-driven model provides a better match to the observed slope, but given the systematic uncertainties in metallicity measurements it would be pre-mature to strongly distinguish between the energy and momentum outflow models.

Finally, we note that all of our models result in mass–metallicity relations with small scatter $\simeq 0.06$ dex. Thus, we conclude that outflows are not responsible for the small scatter in the mass–metallicity relation. The origin of this small scatter, as well as the evolution of the mass–metallicity relation, will be discussed in a future paper.

6 HOW DO GALAXIES LOSE THEIR GAS?

Having established that in models with feedback, galaxies lose a significant fraction of their accreted baryons, we now investigate when and how the baryons are lost. The left-hand panels of Fig. 14 show the mass-weighted wind velocity, $V_{\rm w}$, versus the rotation velocity at 2.2 disc scalelengths, $V_{2.2I}$, for models at redshifts $z = 0.0$, 1.4 and 3.0. This relation has a slope $\simeq$1, small scatter and holds at all redshifts. For both energy- and momentum-driven winds, the mean wind velocity is roughly 2.5–3 times $V_{2.2I}$. However, this relation is no surprise, since by construction we assume that the local wind velocity is equal to the local escape velocity. The non-zero scatter in the relation between $V_{\rm w}$ and $V_{2.2I}$ is due to the fact that, in our model, mass is ejected from a range of radii, and hence a range of escape velocities.

The middle panels of Fig. 14 show the relation between wind velocity and stellar mass. For galaxies in the mass range $10^{9.6} < M_{\rm star} < 10^{10.8}\,{\rm M}_{\odot}$, this relation has a slope of $\simeq$0.33 $\pm$ 0.01 for all redshifts and both wind models. For the energy wind model, this relation has a shallower slope at low stellar masses. The slope and small scatter of this relation are a consequence of the tight correlation between $V_{\rm w}$ and $V_{2.2I}$, and the small scatter in the stellar mass TF relation (Figs 6 and 7). The zero-point of the relation between wind velocity and stellar mass evolves with redshift, which is a reflection of lower stellar masses at a given rotation velocity in higher redshift galaxies. Note that this implies evolution in the zero-point of the stellar mass TF relation, which will be discussed in a future paper.

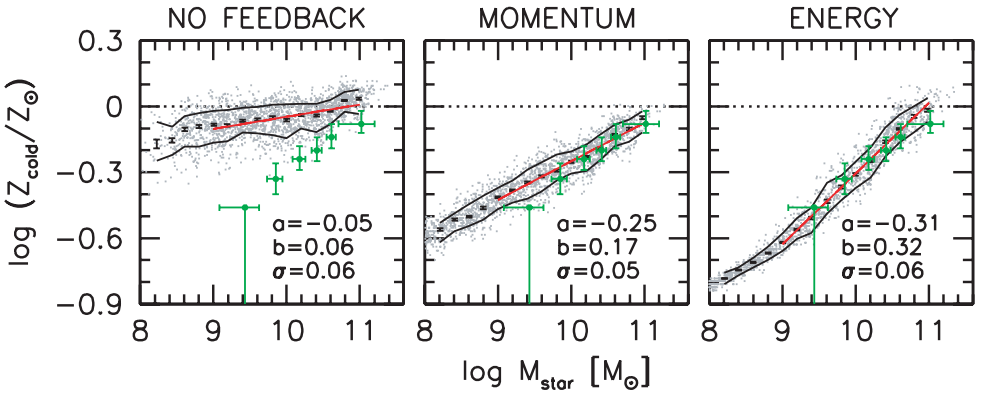

Figure 13. Dependence of the mass–metallicity relation at $z = 2.26$ on feedback. The black lines show the 16th and 84th percentiles of metallicity in bins of width 0.25 dex in $M_{\rm star}$. The red lines show a fit of the form: $\log(Z_{\rm cold}/{\rm Z}_{\odot}) = a + b(\log M_{\rm star} - 10)$. The zero-point, slope and scatter for each fit are given in the lower-right corner of each panel. The green points show observational data at $z = 2.26 \pm 0.17$ from Erb et al. (2006). The model without feedback overpredicts the metallicities, whereas the models with feedback provide good matches to the observations.

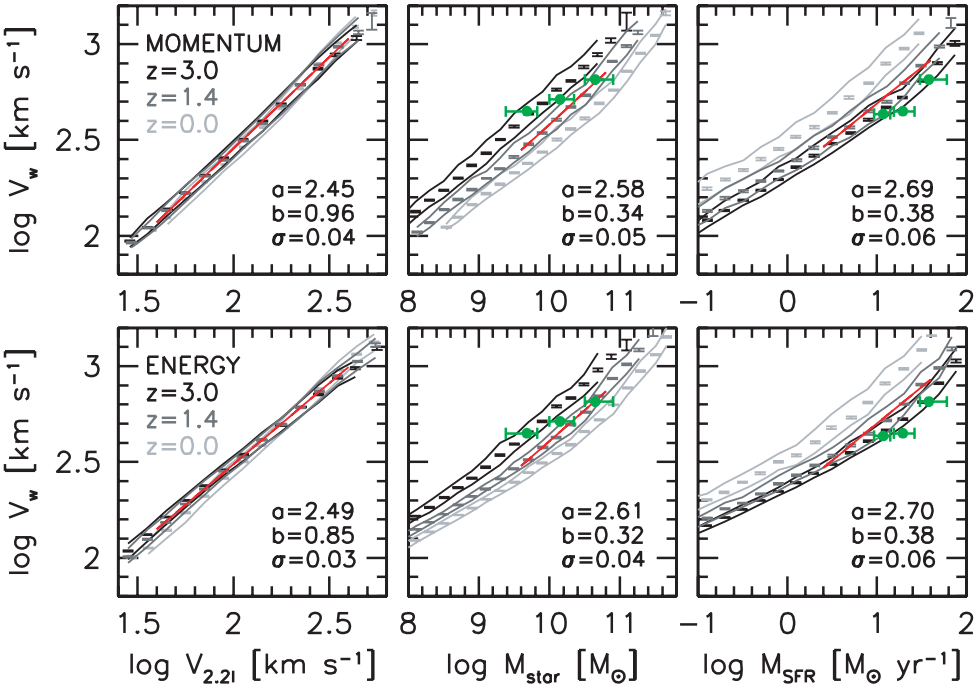

Figure 14. Mass-weighted wind velocity, $V_{\rm w}$, versus galaxy rotation velocity, $V_{2.2I}$, stellar mass, $M_{\rm star}$, and SFR, $\dot{M}_{\rm star}$, for energy-driven (lower panels) and momentum-driven (upper panels) wind models. The black and grey lines show the 16th and 84th percentiles of the models at $z = 0.0$ (light grey), 1.4 (dark grey) and 3.0 (black). The red lines show fits to the $z = 1.4$ models. The fits are of the form: $\log V_{\rm w} = a + b\,(\log V_{2.2I} - 2)$, $a + b\,(\log M_{\rm star} - 10)$ and $a + b\,(\log M_{\rm SFR} - 1)$. The slopes ($b$), zero-points ($a$) and scatter ($\sigma$) of these fits are given in the lower-right corner of each panel. The green points with error bars show observational data at $z \simeq 1.4$ from Weiner et al. (2009) (see text for further details). Both energy- and momentum-driven wind models predict similar scalings that are broadly in agreement with the observations.

The right-hand panels of Fig. 14 show the relation between wind velocity and SFR. This relation has a slope $\simeq$0.38 $\pm$ 0.01 at $z = 1.4$ for both wind models. Galaxies at $z = 1.4$ and 3.0 have similar zero-points, but galaxies at $z = 0.0$ have lower SFRs at a given wind velocity.

Overplotted in red in Fig. 14 are the observational results at $z \simeq 1.4$ for the wind velocity versus stellar mass and SFR from Weiner et al. (2009). These results are based on a sample of 1406 galaxy spectra from the Deep Extragalactic Evolutionary Probe 2 (DEEP2) redshift survey (Davis et al. 2003) which have both [O II] 3727 emission lines (to provide secure redshifts) and Mg II $\lambda\lambda$ 2796, 2803 Å absorption lines (to probe low-ionization outflowing gas). For the wind velocity, we adopt the velocity where Mg II absorption is at 10 per cent of the continuum.

The slope of the wind-velocity–stellar-mass relation is shallower in the data than our models. However, the slope of the wind velocity SFR is consistent. The differences between the slopes of the wind-velocity–stellar-mass relation of the models and data may be caused by a bias against low-mass low SFR galaxies in the observations. Martin (2005) find a similar scaling between wind velocity and SFR in low-redshift ultraluminous infrared galaxies. Thus both energy and momentum wind models predict scalings that are broadly consistent with the observations. This agreement is primarily due to our assumption that the wind velocity is equal to the local escape velocity. It is surprising that such a naive assumption, which is most likely incorrect, is in good agreement with the observations.

We have shown that the energy- and momentum-driven wind models predict very similar scalings between wind velocity and stellar mass and SFR. The slopes of these relations are only significantly different at low masses and low SFRs. Fig. 15 shows the mass loading factor versus wind velocity for the momentum- and energy-driven wind models. The relations from our galaxy formation models are independent of redshift, and close to the expected relations (shown as red lines in Fig. 15) for a model where the wind velocity is independent of radius. For a wind velocity of $\simeq$100 km s^{-1}, the mass loading factor of the energy wind model is an order of magnitude higher than that of the momentum wind model. Thus observationally, it may be easier to distinguish between energy- and

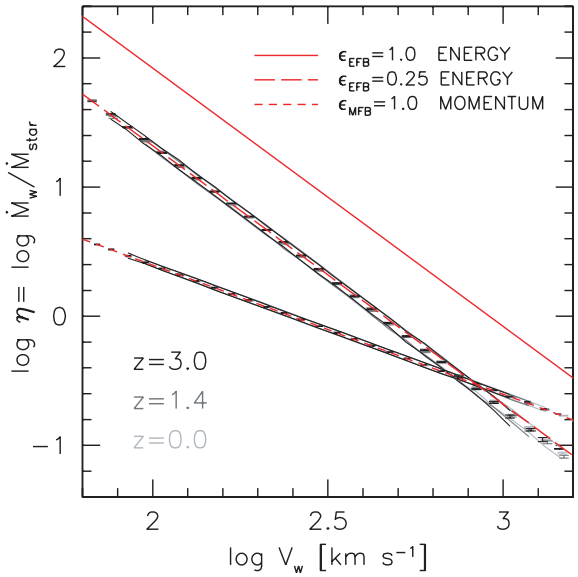

Figure 15. Mass loading factor versus mean (outflow mass-weighted) wind velocity for our energy- and momentum-driven wind models at redshifts $z = 0.0$, 1.4 and 3.0. The red lines are as in Fig. 4.

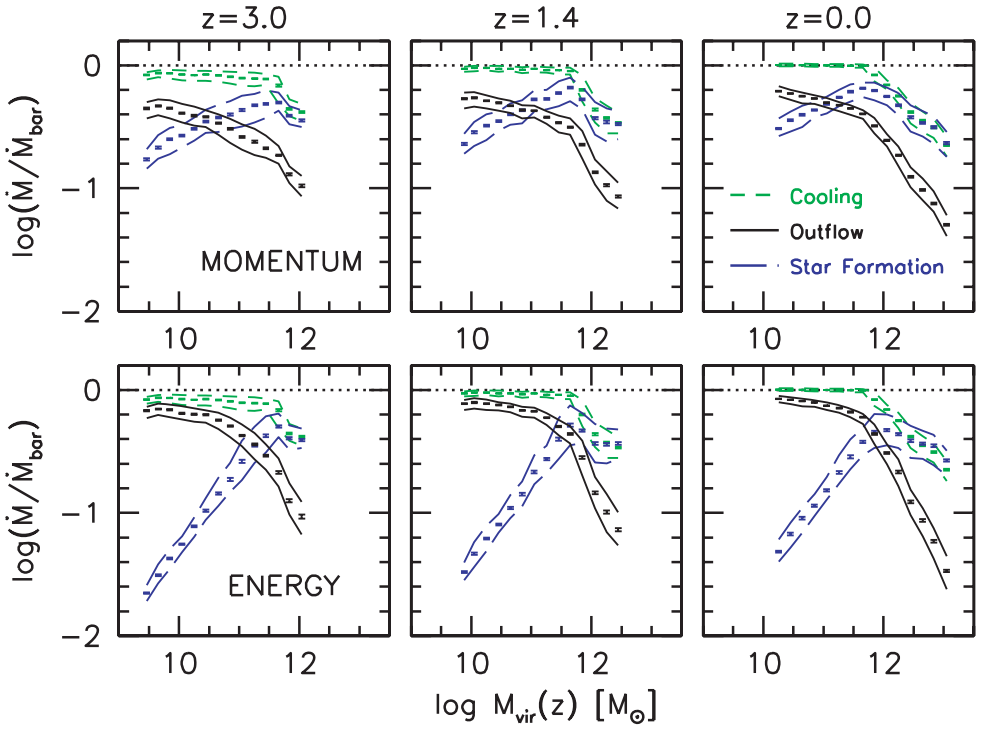

Figure 16. Ratio between rate of cooling (green), SF (blue) and outflow (black) to the rate of baryon accretion as a function of virial mass. The upper panels are for momentum-driven winds, the lower panels for energy-driven winds. The panels from the left to right are for models at redshift 3.0, 1.4 and 0.0, respectively. For haloes below $\simeq 1 \times 10^{12}\,\mathrm{M}_{\odot}$, the cooling rate is essentially equal to the baryon accretion rate. The relative SFR increases with halo mass, whereas the relative outflow rate shows exactly the opposite trend. Thus globally the outflow rate is dominated by the depth of the potential well, rather than the efficiency of SF. Outflow rates are higher for energy-driven winds due to the higher mass loading factor, this results in lower mass and surface density galaxies, and hence lower relative SFRs.

momentum-driven winds by measuring the mass loading factors of low-mass galaxies.

6.1 Relation between outflows, inflows and star formation

Fig. 16 shows the ratio between rate of cooling, SF and outflow to that of baryon accretion, versus halo mass, at redshifts $z = 3.0$ (left-hand panels), 1.4 (middle panels) and 0.0 (right-hand panels). In our model, the baryon accretion rate is the cosmic baryon fraction times the halo accretion rate, which is a function of the redshift zero halo mass and concentration. Thus higher mass haloes have higher rates of baryon accretion.

Cooling is efficient in haloes below $\simeq 10^{12}\,\mathrm{M}_{\odot}$, so that the rate of cooling is almost equal to the rate of baryon accretion. Above $\simeq 10^{12}\,\mathrm{M}_{\odot}$, the cooling efficiency drops, and thus the rate of cooling drops significantly below the rate of baryon accretion. The scatter in the cooling rate is caused by scatter in the halo concentration, which effects the density of the halo and hence temperature of the hot gas.

The SFR, relative to the cooling rate, increases with halo mass, with a much stronger dependence in energy-driven winds than momentum-driven winds. Above $10^{12}\,\mathrm{M}_{\odot}$, the relative SFR decreases, but this is due to the decline in the cooling rate, rather than inefficient SF. The relative outflow rate shows the opposite trend. Outflows are more efficient in lower mass haloes, this is despite the lower relative SFRs. For haloes with $M_{\rm vir} \lesssim 10^{12}\,\mathrm{M}_{\odot}$, the energy wind model has higher outflow rates than the momentum wind model. This is due to the higher mass loading factor in the energy wind model, which can be of the order of $\sim$10 in low-mass haloes.

7 SUMMARY

We use a disc galaxy evolution model to investigate the impact of mass outflows (a.k.a. feedback) on disc galaxy scaling relations, galaxy mass fractions and spin parameters. Our model follows the accretion, cooling, SF and ejection of mass inside growing dark matter haloes with cosmologically motivated AMDs. In our models, the surface density profile of the baryonic disc is determined by the specific AMD of the cooled baryons and by the assumption of centrifugal equilibrium. The surface density profile of the stellar disc is then determined by the efficiency of SF with gas density. We model SF with a Schmidt law on the dense molecular gas. We compute the molecular fraction using the pressure-based prescription in Blitz & Rosolowsky (2006). We consider both energy- and momentum-driven galaxy wind models. For both models, we assume that the wind velocity is equal to the local escape velocity (from the disc and halo). This assumption maximizes the amount of mass loss. Our main conclusions are summarized as follows.

(i) *Velocity–mass–radius scaling relations:* models without feedback result in discs that, at a given stellar mass, are too small and rotate too fast (Figs 2 and 5). With increasing feedback efficiency, discs become larger and rotate slower (Fig. 2). With high feedback efficiency, discs are too large at a given stellar mass. However, the offset from the TF relation is almost independent of feedback, because feedback reduces both the stellar mass and rotation velocity (Fig. 2).

(ii) *TF zero-point:* models with halo contraction overpredict the zero-point of the stellar-mass–velocity relation, independent of the feedback efficiency (Figs 2 and 3). Models without halo

contraction result in a better agreement, but still overpredict the rotation velocities at high stellar masses (Figs 2 and 3).

(iii) *The BTF relation:* the BTF relation, defined as the relation between the (cold) baryonic mass and the circular velocity at large radius in the gas disc, is only weakly sensitive to the feedback model (Fig. 8). In particular, our energy-driven feedback model (which results in galaxy mass fractions decreasing with decreasing halo mass) yields an almost identical slope to the no feedback model (which in which galaxy mass fractions are constant with halo mass).

(iv) *Gas fractions versus stellar mass:* models without feedback predict gas fractions that are too low (Fig. 12), which is a result of the discs having densities that are too high, which in turn results in SF being too efficient. Models with feedback predict gas fractions in good agreement with observations (Fig. 12).

(v) *Mass fractions versus halo mass:* without feedback, cooling is very efficient below a halo mass of $\simeq 10^{12}\,\mathrm{M}_{\odot}$ (Fig. 9). Below this mass, the galaxy formation efficiency (defined as the percentage of universal baryons that ends up as stars and cold gas, i.e. $m_{\rm gal}/f_{\rm bar}$) is constant at $\simeq$95 per cent, while above this mass, galaxy formation efficiency decreases. In both energy and momentum feedback models, mass is more easily ejected from lower mass haloes, resulting in galaxy mass fractions that increase with halo mass (below the cooling threshold). Maximum galaxy formation efficiencies occur at a virial mass of $M_{\rm vir} \simeq 10^{12}\,\mathrm{M}_{\odot}$. Maximum efficiencies as low as $\simeq$35 per cent can be produced with energy-driven winds with a feedback efficiency of 0.25. However, even with a feedback efficiency of 1, momentum-driven winds result in maximum galaxy formation efficiencies of $\simeq$50 per cent (see below for further discussion).

(vi) *Mass fractions versus spin parameter:* at a given halo mass, higher density discs are more efficient at removing mass (Fig. 11): i.e. energy/momentum input is more important than depth of potential, inconsistent with assumption of Gnedin et al. (2007). At a given halo mass, SF is more efficient in galaxies with higher surface densities, thus gas fractions are lower. This helps to reduce the surface density dependence of the stellar mass TF relation relative to the baryonic TF relation (as argued by Firmani & Avila-Reese 2000; van den Bosch 2000; D07).

(vii) *Spin parameter of baryons versus dark matter:* in haloes with masses lower than $\simeq 10^{12}\,\mathrm{M}_{\odot}$, the galaxy spin is higher than halo spin, because feedback preferentially removes low-angular-momentum material (Fig. 9). In haloes more massive than $\simeq 10^{12}\,\mathrm{M}_{\odot}$, the galaxy spin is lower than halo spin, because the gas that has not cooled has the highest specific angular momentum. At a given halo mass, the spin of the galaxy is tightly correlated with the spin of the halo, i.e. the parameter $(j_{\rm gal}/m_{\rm gal})$ has a scatter of only $\simeq 0.02 - 0.04$ dex (Fig. 10). This tight correlation is true even for galaxies that have lost over 80 per cent of their baryons. However, due to the density dependence of SF, the parameter $(j_{\rm star}/m_{\rm star})$ has a larger scatter of $\simeq$0.08 dex (see below for further discussion).

(viii) *Spin parameter of baryons versus stars:* the spin of the stars is always less than the spin of the baryons because SF is more efficient at smaller radii. Below $M_{\rm vir} \simeq 10^{12}\,\mathrm{M}_{\odot}$, the median spin parameter of the stars is roughly independent of halo mass (Fig. 9).

(ix) *Wind velocity versus Galaxy observables:* both feedback models result in tight correlations among the mean wind velocity, $V_{\rm w}$, stellar mass, $M_{\rm star}$, and SFR, $\dot{M}_{\rm star}$: $V_{\rm w} \propto 3V_{2.2I} \propto M_{\rm star}^{0.33} \propto \dot{M}_{\rm star}^{0.38}$ (Fig. 14). The first relation is essentially construction, since we assume the wind velocity is equal to the local escape velocity from the galaxy–halo system. The second and third relations are non-trivial. The scaling relations between wind velocity and stellar mass/SFR are broadly consistent with observations at $z \sim 1.4$ from the DEEP2 redshift survey (Weiner et al. 2009).

(x) *Differences between energy- and momentum-driven winds:* the main difference is the mass loading factor, which scales like $V_{\rm w}^{-2}$ for energy-driven winds and $V_{\rm w}^{-1}$ for momentum-driven winds. For equal fractions of the initial energy/momentum from the SN that drives the outflow, energy-driven winds have higher mass loading factors for all relevant wind velocities. The differences between the mass loading factors increase with decreasing wind velocity (Fig. 4). Thus energy-driven winds are much more efficient at removing mass from lower mass haloes (Fig. 9). This has at least three observational consequences: (1) different slopes of the size–stellar-mass relation ($\simeq$0.14 for energy, Fig. 7, and $\simeq$0.28 for momentum, Fig. 6); (2) different slopes of the relations between $m_{\rm gal}$ and $m_{\rm star}$ with $M_{\rm vir}$ (see Table 2) and (3) different slopes in the metallicity–stellar-mass relation at $z \simeq 2$ ($\simeq$ 0.17 for momentum and $\simeq$0.33 for energy, Fig. 13) (see below for further discussion).

(xi) *Outflow versus inflow:* the median mass outflow rate relative to the median mass inflow rate *decreases* with increasing halo mass, whereas the median SFR relative to the median inflow rate *increases* with increasing halo mass (Fig. 16). Thus, globally, the depth of the potential is more important than the energy/momentum input from SN.

7.1 Comments on galaxy spin versus halo spin

The assumption that $\lambda_{\rm gal} = \lambda$ (i.e. $j_{\rm gal}/m_{\rm gal} = 1$) underlies almost all analytical and semi-analytical models of disc galaxy formation (e.g. Dalcanton et al. 1997; MMW; Somerville & Primack 1999; Cole et al. 2000; Firmani & Avila-Reese 2000; Croton et al. 2006; D07; Somerville et al. 2008). We have shown that this assumption is no longer valid in models with outflows. A similar conclusion was reached by Maller & Dekel (2002).

The result that $\lambda_{\rm gal}$ is significantly higher than λ in low-mass haloes helps to resolve the puzzle surrounding the spin parameters of bulge-less dwarf galaxies. Using observations of 14 late-type dwarf galaxies, van den Bosch et al. (2001) found the distribution of $\lambda_{\rm gal}$ to have a median of $\simeq$0.06. D'Onghia & Burkert (2004) measured the spin parameter of dark matter haloes that are most likely to host bulge-less disc galaxies, and found a median spin parameter $\bar{\lambda} \simeq 0.028$ (after correcting to the energy definition of halo spin). D'Onghia & Burkert (2004) assumed that in the best case scenario $\lambda_{\rm gal} = \lambda$, and thus there is a discrepancy of a factor of $\simeq$2 between the observed and predicted spin parameters. However, with energy-driven feedback, our models produce galaxy spin parameters a factor of 2 higher than the halo spin parameters in low-mass haloes, thus resolving the discrepancy.

7.2 Comments on energy- versus momentum-driven winds

In our models, energy- and momentum-driven winds result in significantly different slopes of the relations between disc size and stellar mass. Observations of the size–stellar-mass relation for late-type galaxies from Shen et al. (2003) find a slope of 0.14 at the low-mass end, which favours our energy wind model over our momentum wind model. However, at the high-mass end, a number of authors find steeper slopes (e.g. Shen et al. 2003; Pizagno et al. 2005; Courteau et al. 2007), which is in better agreement with our momentum wind model. However, there are a number of uncertainties in the observations (such as determinations of stellar masses, inclination effects on galaxy sizes) which need to be quantified before firmer conclusions can be made.

Our energy- and momentum-driven wind models also result in significantly different slopes to the relations between galaxy mass,

stellar mass and halo mass. These relations can, in principle, be directly tested with galaxy–galaxy weak lensing and/or satellite kinematics.

7.3 Comments on why galaxy formation is inefficient

Observations of halo masses from weak lensing studies (e.g. Hoekstra et al. 2005; Mandelbaum et al. 2006) and methods that match the stellar mass function to the halo mass function (e.g. Yang et al. 2007; Conroy & Wechsler 2008) find that the peak galaxy formation efficiency has to be relatively low $\simeq$0.33. We have shown that low galaxy formation efficiencies are also required to explain the zero-points of the relations among velocity, stellar mass and size of disc galaxies.

We have shown that mass ejection through SN-driven winds provides at least a partial explanation for this. However, by assuming that the wind velocity is equal to the local escape velocity results in maximal outflow rates for a given energy/momentum input. While such a scaling of wind velocity with galaxy escape velocity is at least supported by observations at low and high redshift, galactic winds will likely have a range of velocities, which will reduce the outflow rates from those in our model. Needless to say, the scaling between wind velocity and escape velocity, as well as the mass loading factor, needs to be investigated further with hydrodynamical simulations.

Even though we have adopted a maximally efficient mass outflow model, we still need to use 25 per cent of all SN energy (or 100 per cent of all SN momentum) in order to eject enough mass to fit the data. It remains to be seen whether such high efficiencies are realistic or not. This requires detailed hydrodynamical simulations with radiative transfer that accurately model the complicated multiphase structure of the ISM. It is likely that one needs to invoke additional mechanisms to explain the low baryonic mass fractions observed in galaxy mass haloes.

An alternative explanation for low galaxy formation efficiencies is that most of the baryons never accrete on to galaxies in the first place. In massive haloes $M_{\rm vir} \gtrsim 10^{12}\,{\rm M}_{\odot}$ (in which gas is heated by an accretion shock), accretion on to the galaxy could be suppressed with multiphase cooling (Maller & Bullock 2004) or additional heating such as from AGN or mergers. However, in low-mass haloes, most of the baryons are accreted in cold streams. Rather than disrupting these streams from the outside, such as with feedback from the central galaxy, a more likely scenario would be to disrupt them from the inside, i.e. by reheating baryons and ejecting them from the cold flow into the intergalactic medium, *before* the cold flow reaches the halo. We have shown that even though the SF efficiency is much lower in lower mass haloes, the mass loading factor is typically high, especially for energy-driven winds. Thus even small amounts of star formation in low-mass haloes could be sufficient to significantly reduce the baryon accretion rate, and hence baryon mass fraction of the main galaxy. Coupled with outflows from the main galaxy, this could result in galaxy mass fractions in better agreement with observations, but with a lower (and more realistic) conversion efficiency of SN energy/momentum into galactic winds than required by our current models.

ACKNOWLEDGMENTS

We thank Eric Bell, Neil Katz, Andrea Macciò, Julio Navarro and Padelis Papadopoulous for useful discussions, and the referee for providing useful suggestions for improving the manuscript. AAD acknowledges support from the National Science Foundation Grants AST-0507483, AST-0808133, and the Swiss National Science Foundation (SNF).

REFERENCES

Abadi M. G., Navarro J. F., Steinmetz M., Eke V. R., 2003, ApJ, 591, 499
Avila-Reese V., Zavala J., Firmani C., Hernández-Toledo H. M., 2008, AJ, 136, 1340
Barnes J. E., 1992, ApJ, 393, 484
Bell E. F., de Jong R. S., 2001, ApJ, 550, 212
Bell E. F., McIntosh D. H., Katz N., Weinberg M. D., 2003, ApJS, 149, 289
Benson A. J., Bower R. G., Frenk C. S., Lacey C. G., Baugh C. M., Cole S., 2003, ApJ, 599, 38
Birnboim Y., Dekel A., 2003, MNRAS, 345, 349
Blanton M. R., Geha M., West A. A., 2008, ApJ, 682, 861
Blitz L., Rosolowsky E., 2004, ApJ, 612, L29
Blitz L., Rosolowsky E., 2006, ApJ, 650, 933
Blumenthal G. R., Faber S. M., Flores R., Primack J. R., 1986, ApJ, 301, 27
Bruzual G., Charlot S., 2003, MNRAS, 344, 1000
Bryan G. L., Norman M. L., 1998, ApJ, 495, 80
Bullock J. S., Kolatt T. S., Sigad Y., Somerville R. S., Kravtsov A. V., Klypin A. A., Primack J. R., Dekel A., 2001a, MNRAS, 321, 559
Bullock J. S., Dekel A., Kolatt T. S., Kravtsov A. V., Klypin A. A., Porciani C., Primack J. R., 2001b, ApJ, 555, 240
Chabrier G., 2003, PASP, 115, 763
Cole S., Aragon-Salamanca A., Frenk C. S., Navarro J. F., Zepf S. E., 1994, MNRAS, 271, 781
Cole S., Lacey C. G., Baugh C. M., Frenk C. S., 2000, MNRAS, 319, 168
Conroy C., Wechsler R. H., 2008, preprint (arXiv:0805.3346)
Courteau S., Rix H., 1999, ApJ, 513, 561
Courteau S., Dutton A. A., van den Bosch F. C., MacArthur L. A., Dekel A., McIntosh D. H., Dale D. A., 2007, ApJ, 671, 203
Cox T. J., Dutta S. N., Di Matteo T., Hernquist L., Hopkins P. F., Robertson B., Springel V., 2006, ApJ, 650, 791
Croton D. J. et al., 2006, MNRAS, 365, 11
Dalcanton J. J., Spergel D. N., Summers F. J., 1997, ApJ, 482, 659
Davis M. et al., 2003, in Guhathakurta P., ed., Proc. SPIE Vol. 4834, Science Objectives and Early Results of the DEEP2 Redshift Survey. SPIE, Bellingham, p. 161
de Jong R. S., Bell E. F., 2007, Island Universes – Structure and Evolution of Disk Galaxies. Springer Verlag, Berlin, p. 107
Dekel A., Silk J., 1986, ApJ, 303, 39
Djorgovski S., Davis M., 1987, ApJ, 313, 59
D'Onghia E., Burkert A., 2004, ApJ, 612, L13
Dressler A., Lynden-Bell D., Burstein D., Davies R. L., Faber S. M., Terlevich R., Wegner G., 1987, ApJ, 313, 42
Dunkley J. et al., 2009, ApJS, 180, 306
Dutton A. A., 2009, MNRAS, in press (arXiv:0810.5164)
Dutton A. A., van den Bosch F. C., Dekel A., Courteau S., 2007, ApJ, 654, 27 (D07)
Eke V. R., Baugh C. M., Cole S., Frenk C. S., Navarro J. F., 2006, MNRAS, 370, 1147
Elmegreen B. G., 1993, ApJ, 411, 170
El-Zant A. A., Shlosman I., Hoffman Y., 2001, ApJ, 560, 636
El-Zant A. A., Hoffman Y., Primack J., Combes F., Shlosman I., 2004, ApJ, 607, L75
Erb D. K., Shapley A. E., Pettini M., Steidel C. C., Reddy N. A., Adelberger K. L., 2006, ApJ, 644, 813
Fall S. M., Efstathiou G., 1980, MNRAS, 193, 189
Ferguson A. M. N., Clarke C. J., 2001, MNRAS, 325, 781
Finlator K., Davé R., 2008, MNRAS, 385, 2181
Firmani C., Avila-Reese V., 2000, MNRAS, 315, 457
Gao Y., Solomon P. M., 2004, ApJ, 606, 271
Garnett D. R., 2002, ApJ, 581, 1019
Geha M., Blanton M. R., Masjedi M., West A. A., 2006, ApJ, 653, 240

Gnedin O. Y., Zhao H., 2002, MNRAS, 333, 299
Gnedin O. Y., Weinberg D. H., Pizagno J., Prada F., Rix H.-W., 2007, ApJ, 671, 1115
Governato F., Willman B., Mayer L., Brooks A., Stinson G., Valenzuela O., Wadsley J., Quinn T., 2007, MNRAS, 374, 1479
Hatton S., Devriendt J. E. G., Ninin S., Bouchet F. R., Guiderdoni B., Vibert D., 2003, MNRAS, 343, 75
Hoekstra H., Hsieh B. C., Yee H. K. C., Lin H., Gladders M. D., 2005, ApJ, 635, 73
Holley-Bockelmann K., Weinberg M., Katz N., 2005, MNRAS, 363, 991
Jardel J. R., Sellwood J. A., 2009, ApJ, 691, 1300
Kannappan S. J., 2004, ApJ, 611, L89
Kauffmann G., White S. D. M., Guiderdoni B., 1993, MNRAS, 264, 201
Kennicutt R. C., 1989, ApJ, 344, 685
Kennicutt R. C., 1998, ApJ, 498, 541
Keres D., Katz N., Weinberg D. H., Davé R., 2005, MNRAS, 363, 2
Klypin A., Kravtsov A. V., Valenzuela O., Prada F., 1999, ApJ, 522, 82
Macciò A. V., Dutton A. A., van den Bosch F. C., Moore B., Potter D., Stadel J., 2007, MNRAS, 378, 55
Macciò A. V., Dutton A. A., van den Bosch F. C., 2008, MNRAS, 391, 1940
McGaugh S. S., 2005, ApJ, 632, 859
McGaugh S. S., de Blok W. J. G., 1997, ApJ, 481, 689
McGaugh S. S., Schombert J. M., Bothun G. D., de Blok W. J. G., 2000, ApJ, 533, L99
Magorrian J. et al., 1998, AJ, 115, 2285
Maller A. H., Bullock J. S., 2004, MNRAS, 355, 694
Maller A. H., Dekel A., 2002, MNRAS, 335, 487
Mandelbaum R., Seljak U., Kauffmann G., Hirata C. M., Brinkmann J., 2006, MNRAS, 368, 715
Martin C. L., 2005, ApJ, 621, 227
Milgrom M., 1983, ApJ, 270, 365
Mo H. J., Mao S., White S. D. M., 1998, MNRAS, 295, 319 (MMW)
Mo H. J., Yang X., van den Bosch F. C., Katz N., 2005, MNRAS, 363, 1155
Moore B., Ghigna S., Governato F., Lake G., Quinn T., Stadel J., Tozzi P., 1999, ApJ, 524, L19
Murray N., Quataert E., Thompson T. A., 2005, ApJ, 618, 569
Navarro J. F., Steinmetz M., 2000, ApJ, 538, 477
Navarro J. F., Eke V. R., Frenk C. S., 1996, MNRAS, 283, L72
Navarro J. F., Frenk C. S., White S. D. M., 1997, ApJ, 490, 493
Noordermeer E., Verheijen M. A. W., 2007, MNRAS, 381, 1463
Pelupessy F. I., Papadopoulos P. P., van der Werf P., 2006, ApJ, 645, 1024
Pizagno J. et al., 2005, ApJ, 633, 844
Pizagno J. et al., 2007, AJ, 134, 945
Read J. I., Gilmore G., 2005, MNRAS, 356, 107
Robertson B. E., Kravtsov A. V., 2008, ApJ, 680, 1083
Sakai S. et al., 2000, ApJ, 529, 698
Schaye J., 2004, ApJ, 609, 667
Schmidt M., 1959, ApJ, 129, 243
Sellwood J. A., 2008, ApJ, 679, 379
Sharma S., Steinmetz M., 2005, ApJ, 628, 21 (SS05)
Shen S., Mo H. J., White S. D. M., Blanton M. R., Kauffmann G., Voges W., Brinkmann J., Csabai I., 2003, MNRAS, 343, 978
Somerville R. S., Primack J. R., 1999, MNRAS, 310, 1087
Somerville R. S., Hopkins P. F., Cox T. J., Robertson B. E., Hernquist L., 2008, MNRAS, 391, 481
Spergel D. N. et al., 2007, ApJS, 170, 377
Stringer M. J., Benson A. J., 2007, MNRAS, 382, 641
Sutherland R. S., Dopita M. A., 1993, ApJS, 88, 253
Tollerud E. J., Bullock J. S., Strigari L. E., Willman B., 2008, ApJ, 688, 277
Tonini C., Lapi A., Salucci P., 2006, ApJ, 649, 591
Toomre A., 1964, ApJ, 139, 1217
Tully R. B., Fisher J. R., 1977, A&A, 54, 661
van Albada T. S., Sancisi R., 1986, Phil. Trans. R. Soc. A, 320, 447
van den Bosch F. C., 1998, ApJ, 507, 601
van den Bosch F. C., 2000, ApJ, 530, 177
van den Bosch F. C., 2001, MNRAS, 327, 1334
van den Bosch F. C., 2002a, MNRAS, 332, 456
van den Bosch F. C., 2002b, MNRAS, 331, 98
van den Bosch F. C., Burkert A., Swaters R. A., 2001, MNRAS, 326, 1205
Verheijen M. A. W., 2001, ApJ, 563, 694
Wechsler R. H., Bullock J. S., Primack J. R., Kravtsov A. V., Dekel A., 2002, ApJ, 568, 52
Weinberg M. D., Katz N., 2002, ApJ, 580, 627
Weiner B. J. et al., 2009, ApJ, 692, 187
Weinzirl T., Jogee S., Khochfar S., Burkert A., Kormendy J., 2009, ApJ, in press
Wong T., Blitz L., 2002, ApJ, 569, 157
Wu J., Evans N. J. II, Gao Y., Solomon P. M., Shirley Y. L., Vanden Bout P. A., 2005, ApJ, 635, L173
Yang X., Mo H. J., van den Bosch F. C., Pasquali A., Li C., Barden M., 2007, ApJ, 671, 153
Zhao D. H., Mo H. J., Jing Y. P., Börner G., 2003, MNRAS, 339, 12

This paper has been typeset from a TEX/LATEX file prepared by the author.